JOURNAL OF GEOPHYSICAL RESEARCH: SOLID EARTH, VOL. 118, 5320–5338, doi:10.1002/jgrb.50370, 2013

Analysis of teleseismic *P* waves with a 5200-station array in Long Beach, California: Evidence for an abrupt boundary to Inner Borderland rifting

Brandon Schmandt[1,2] and Robert W. Clayton[2]

Received 14 April 2013; revised 23 August 2013; accepted 9 September 2013; published 3 October 2013.

[1] We analyze teleseismic *P* waves from four Mw ≥ 6.5 earthquakes recorded by a petroleum industry survey in Long Beach, California. The survey used a 2-D array with up to 5200 seismometers, 120 m mean spacing, and 7 – 10 km aperture. At frequencies near 1 Hz, *P* wave travel times and amplitudes exhibit coherent lateral variations over scales as short as ~400 m, including locally delayed travel times and increased amplitudes at the crest of the Long Beach anticline. Deeper heterogeneity is indicated by *P* wave phase velocities that deviate from reference model predictions for events from southwestern azimuths. We postulate that a sharp northeastward increase in Moho depth from the Inner Borderland (IB) to mainland southern California causes the anomalous phase velocities. Elastic forward modeling finds the travel times are fit well by a Moho that dips 65° to the northeast and flattens ~10 km southwest of the Newport-Inglewood fault zone. Constraining the felsic thickness of mainland crust to 28 km requires an 8 km thick layer with a P-velocity of 7 km/s beneath it, which could result from basal accretion of former Farallon ocean crust or magmatic underplating during Miocene volcanism. Forward models with a 65° Moho dip predict a P-to-s conversion with a phase velocity of ~5 km/s. Deconvolution of the array's mean *P* wave signal isolates a similar later arriving phase. The steep crust thickness transition supports a locally abrupt boundary to IB rifting. Our results highlight the utility of dense short-period arrays for passive imaging at near surface to uppermost mantle depths.

Citation: Schmandt, B., and R. W. Clayton (2013), Analysis of teleseismic *P* waves with a 5200-station array in Long Beach, California: Evidence for an abrupt boundary to Inner Borderland rifting, *J. Geophys. Res. Solid Earth*, *118*, 5320–5338, doi:10.1002/jgrb.50370.

1. Introduction

[2] Structural imaging with teleseismic body waves typically relies on data from arrays of broadband seismometers deployed about 5 – 100 km apart [e.g., *Lerner-Lam et al.*, 1998; *van der Hilst et al.*, 1994; *Nabelek et al.*, 1993; *Levander et al.*, 1999]. Here we employ an unusual array for analysis of teleseismic *P* waves. This array, referred to as the Long Beach array, has a nominal station spacing of about 120 m and was designed for active source exploration of petroleum resources rather than teleseismic imaging. It occupied over 5200 sites with 10 Hz vertical component seismometers in the heavily urbanized area of Long Beach, CA (Figure 1). This location in an active zone of distributed deformation between the Pacific and North America plates provides an exceptional opportunity to investigate the lithospheric imaging potential of teleseismic sources recorded by dense short-period arrays. The Pacific-Farallon spreading ridge first entered the western North America subduction zone near this latitude about 28 Ma [*Atwater and Stock*, 1998]. Subsequent subduction termination and development of the modern San Andreas fault system resulted in dissection of the former forearc and arc provinces through translation and rotation of crustal blocks, extension, and localized compression [*Hornafius et al.*, 1986; *Legg*, 1991; *Powell*, 1993; *Bird and Rosenstock*, 1984]. The result is a patchwork of distinct crustal provinces and a complex system of faults that distributes Pacific-North America deformation from the Continental Borderland to eastern California [e.g., *Meade and Hager*, 2005].

[3] The Long Beach array sits at the outboard transition from mainland southern California to the highly extended and submerged crust of the Inner Borderland. Miocene sediments and volcanic rocks comprise the surface of most of the Inner Borderland and the Catalina schist is its dominant basement lithology [*Vedder et al.*, 1979; *Bohannon and Geist*, 1998]. Petrology and geochronology investigations identify the Catalina schist as a derivative of the Franciscan subduction complex that was metamorphosed in the Mesozoic forearc at 25 – 45 km depth and exhumed to

[1]Department of Earth and Planetary Sciences, University of New Mexico, Albuquerque, New Mexico, USA.
[2]Seismological Laboratory, California Institute of Technology, Pasadena, California, USA.

Corresponding author: B. Schmandt, Department of Earth and Planetary Sciences, University of New Mexico, Albuquerque, NM 87131, USA. (bschmandt@unm.edu)

2169-9313/13/10.1002/jgrb.50370

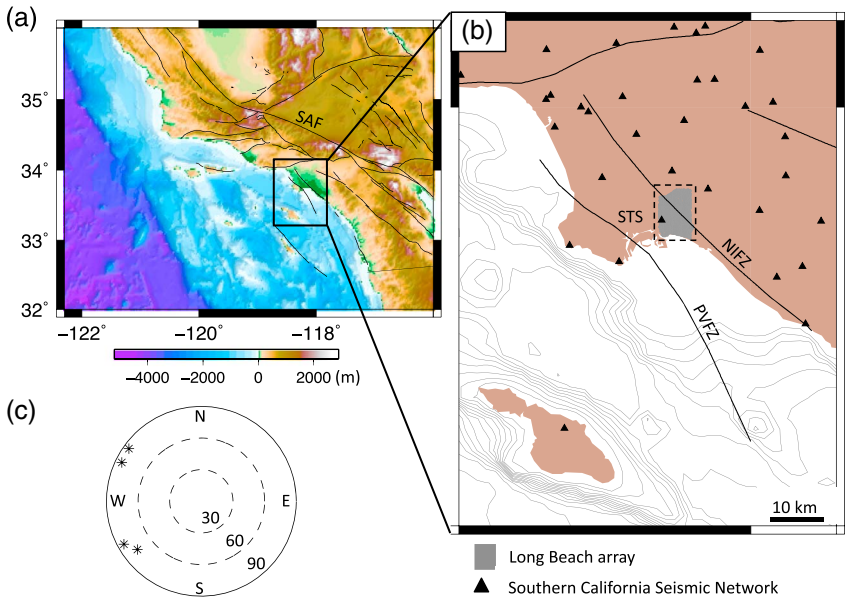

Figure 1. Array location and teleseismic sources. (a) Regional map of southern California and the Continental Borderland. Mapped fault locations are from *Jennings and George* [1994], and the San Andreas fault is labeled (SAF). (b) Local map with the stations of the Long Beach array (gray) and Southern California Seismic Network (black triangles). The Newport-Inglewood fault zone (NIFZ), Palos Verde fault zone (PVFZ), and permanent broadband station STS are labeled. (c) Distance and back azimuth of teleseismic *P* wave sources (black asterisks) with respect to the Long Beach array. The black dashed box outlines the area plotted in Figures 4–8.

depths of 10 – 15 km by the middle Cretaceous [*Platt*, 1976; *Grove and Bebout*, 1995]. It is debated whether or not the Catalina schist of the Inner Borderland is floored by oceanic lithosphere that stalled during plate margin transformation from subduction to right-lateral transform [e.g., *ten Brink et al*. 2000; *Nazareth and Clayton*, 2003]. Tectonic reconstructions constrained by measurements of paleomagnetism require a high degree of extension in the Inner Borderland since about 18 Ma to accommodate >100° of clockwise rotation of the western Transverse Ranges [*Hornafius et al*., 1986; *Luyendyk*, 1991]. An important driving force for block rotation of the western Transverse Ranges (WTR) is thought to be basal traction imposed by a stalled Farallon slab fragment attached to the Monterey microplate and consequently captured by the Pacific plate in the Miocene [*Nicholson et al*., 1994]. High lower crustal shear velocities beneath the WTR are resolved by regional waveform tomography and may represent a fragment of former Farallon ocean crust fused to the bottom of the WTR [*Tape et al*., 2009]. In the wake of WTR rotation, contemporary crust thickness in the Inner Borderland is 19 – 23 km [*ten Brink et al*., 2000; *Richards-Dinger and Shearer*, 1997; *Zhu and Kanamori*, 2000; *Yan and Clayton*, 2007a], in contrast to average crustal thickness of about 30 km in mainland southern California [*Tape et al*., 2012].

[4] In a more local context, the Long Beach array overlaps part of the transpressional Newport-Inglewood fault zone (NIFZ; Figure 1). The array is approximately centered on Signal Hill, which is the highest part of the Long Beach anticline [*Wright*, 1991]. Productive oil fields are distributed along the NIFZ and Signal Hill is a classic example of an anticlinal petroleum trap [*Wright*, 1991]. Aside from its importance for the location of petroleum reservoirs, the NIFZ near the latitude of Long Beach may delimit the eastern boundary of Inner Borderland rifting because well data show that it juxtaposes deeply exhumed Catalina schist against granitic basement rocks to the east [*Yerkes et al*., 1965; *Wright*, 1991]. The NIFZ is also of importance for seismic hazard. It hosts frequent small earthquakes (Mw < 3) with focal depths that cluster between 6 and 11 km [*Hauksson*, 1987], and its last major earthquake was the very destructive Mw-6.4 Long Beach earthquake in 1933 [*Hauksson and Gross*, 1991].

[5] Recent analysis demonstrates that the continuous data from the dense Long Beach array can provide new constraints on local structure. Application of ambient noise Rayleigh wave tomography at frequencies between 0.5 and 4 Hz affords a detailed view of shear velocity structure and azimuthal anisotropy to a depth of 800 m beneath the Long Beach array [*Lin et al*., 2013]. Rayleigh wave tomography images a northward decrease in shear velocity contrast across the NIFZ at depths of ≤ 500 m and high velocities straddling the NIFZ near Signal Hill at depths of 500 – 800 m [*Lin et al*., 2013]. Different types of passive source data may provide new insight into deeper structure.

[6] Here we explore the potential of teleseismic *P* waves recorded by the Long Beach array for locally probing lithospheric structure. Mean instrument spacing within the array, ~120 m, is two orders of magnitude smaller than in the most densely covered part of the Southern California Seismic Network (SCSN), but the Long Beach array has a maximum aperture of only about 10 km (Figure 1). So the data offer a chance to investigate the small-scale limit of structural heterogeneity illuminated by ~1 Hz teleseismic *P* waves.

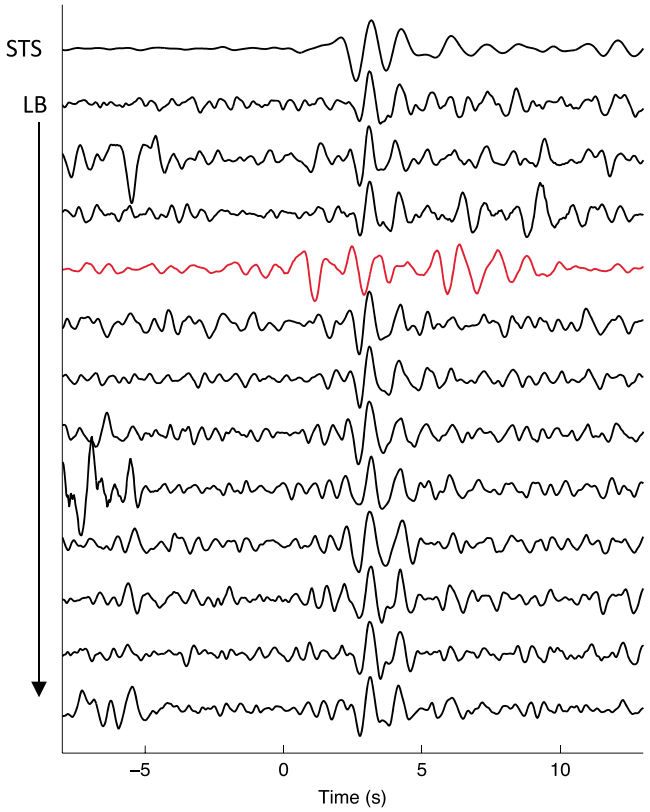

Figure 2. Comparison of Southern California Seismic Network broadband station STS and 14 stations from the Long Beach array that are within 400 m of STS for event 2. The location of STS is shown in Figure 1b. All waveforms were band pass filtered from 0.4 to 1.5 Hz and normalized by the maximum amplitude of the *P* wave arrival. The red trace is an example that was rejected by visual inspection.

We measure relative travel time residuals and amplitudes of *P* waves from four Mw ≥ 6.5 earthquakes. Additionally, we use the dense array data to form an effective source estimate and deconvolve it from each seismogram in the array to evaluate the potential for identification of scattered phases with only vertical component teleseismic data from a narrow aperture array. We find coherent lateral variations in travel time residual and amplitude over length-scales as short as about 400 m. An anomalous trend in travel time residuals as a function of distance is observed only for events from the southwest and indicates a sharp lateral contrast in structure in that direction. We test whether idealistic forward models of increasing crust thickness at the edge of the Inner Borderland can explain the anomalous phase velocity of *P* waves from the southwest. Travel time data are fit by a surprisingly steep 65° transition in Moho depth. Application of array deconvolution isolates scattered arrivals with phase velocity appropriate for a P-to-s conversion from a Moho with 65° dip and lends further support to the existence of a steep structural boundary southwest of the array. These results are discussed in the context of regional structure and as a case study on the lithospheric imaging potential of teleseismic data from arrays composed of a large number of rapidly deployed short-period seismometers.

2. Teleseismic *P* Wave Data

[7] Teleseismic *P* waves from four earthquakes are used to investigate structure near the Long Beach array. Compared to broadband SCSN stations, relatively few teleseismic events produce high quality waveforms in the Long Beach array data. The primary reason is that the seismometers, which are optimized for an active source survey with 8 – 80 Hz vibrating sources, have a 10 Hz corner frequency. Additionally, a 3 Hz low-cut filter was applied to the data stream, prior to recording to minimize baseline drift of the traces. As a result, instrument sensitivity is about three orders of magnitude below its peak at the frequencies that are optimal for analysis of teleseismic *P* waves in southern California, ~1 Hz. Despite these suboptimal recording characteristics, some teleseismic earthquakes are well recorded by the Long Beach array (Figure 2). Here we focus on four events that produced highly coherent waveforms across the array and occurred at times when at least half the array was active. The waveform data for these events are referenced as *LB3D* [2013] and the digital object identifier provides a link to a website from which the event segments can be downloaded.

[8] Characteristics of the four earthquake sources are taken from the Global Centroid Moment Tensor catalog [*Ekström et al.*, 2012], and are shown in Table 1. The sources include two deep focus Mw-6.5 earthquakes and two shallow subduction zone earthquakes with Mw-9.0 and 6.9. Back azimuths of the events are clustered such that two events arrive from the northwest and two events arrive from the southwest, with ≤10° of azimuth separation in each pair. One shallow and one deep focus event are included in each pair. The total number of seismometers available for each

Table 1. Teleseismic Earthquake Parameters[a]

	Date	Lat.	Lon.	Depth	Mw	Mb	n
Event 1	3/11/2011	37.52	143.05	20	9.1	7.9	5178
Event 2	2/21/2011	−25.95	178.47	567.5	6.5	6.2	2964
Event 3	1/12/2011	26.94	139.94	511.5	6.5	6.3	2760
Event 4	1/13/2011	−20.68	168.34	17.2	6.9	6.6	2843

[a]Table 1 shows the date, estimated hypocenter and magnitude, and number of stations (n) available for each earthquake.

event varies because the Long Beach array seismometers ran entirely on internal battery power and had to be exchanged approximately every 10 – 12 days. The maximum number of stations, 5178, is available for event 1, which is the Mw-9 Tohoku-Oki earthquake of 2011 [*Simons et al*., 2011]. A total of 2760 – 2964 stations are available for events 2 – 4. Hereafter in the text we will refer to the events by their numbers given in Table 1.

3. Relative *P* Wave Travel Times

[9] Data culling is necessary to obtain reliable maps of *P* wave travel time residuals as a result of high cultural noise levels and installation of seismometers in sediment just beneath the surface. All available traces were initially aligned according to the *P* wave arrival predicted by the AK135 global reference model [*Kennett et al*., 1995]. The velocity waveforms were filtered from 0.4 to 1.5 Hz for event 2 and 0.4 to 1.2 Hz for the other three events. A time window around the *P* wave was selected by visual inspection. The root-mean-square (RMS) value of each trace in the *P* wave signal window was compared to the RMS value in a 5 s window preceding the *P* wave onset. Traces were culled if the ratio of the RMS in the signal window to the RMS in the presignal window was less 1.5. Visual inspection was used to remove remaining traces with spurious energy that overlapped with the *P* wave, an example of which is the red trace in Figure 2. Bursts of energy that are not coherent across multiple stations can be reasonably assumed to result from cultural noise. Many seismometers were located within several meters of a road, home, business, or airport runway. Event 2 produced the highest fraction of accepted waveforms (96%) followed by event 1 (87%), event 3 (81%), and event 4 (79%). The accepted waveforms were used for relative travel time analysis.

[10] Relative *P* wave travel time residuals were measured by multichannel cross correlation [*VanDecar and Crosson*, 1990]. The absolute value of nearly all travel time residuals

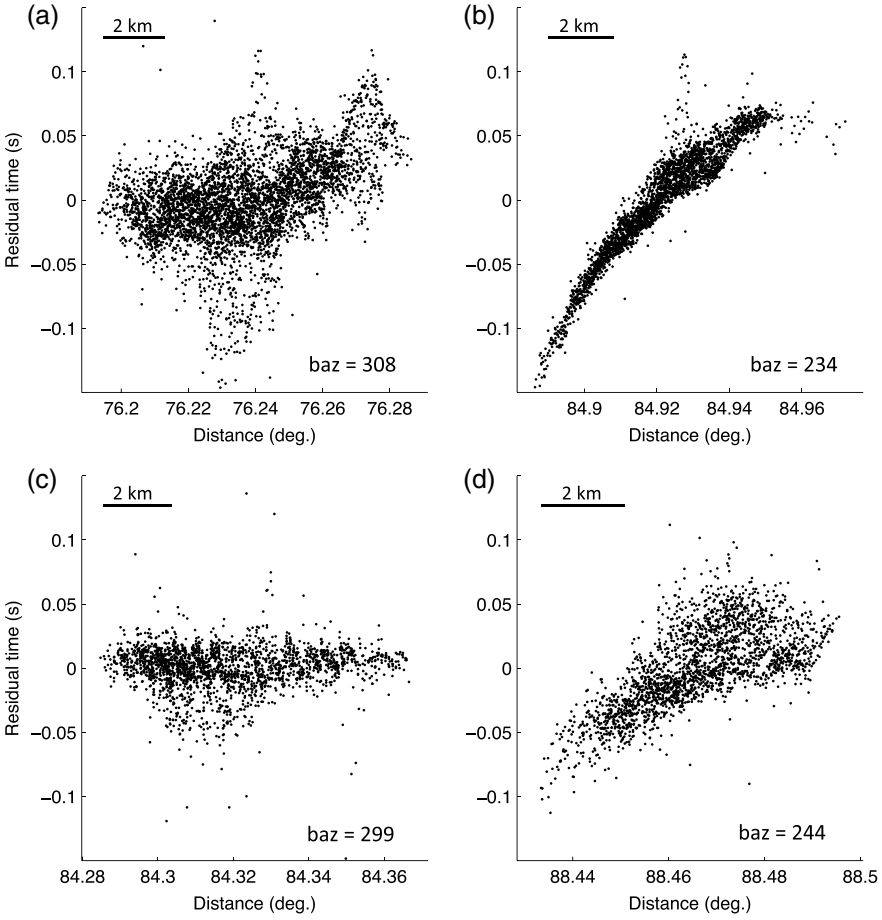

Figure 3. Residual time versus distance for events 1 – 4. Residual times measured by waveform cross correlation are plotted versus distance for events 1 – 4. A trend with slope of zero indicates consistency with the phase velocity predicted by the AK135 velocity model [*Kennett et al*., 1995]. Both events from southwestern azimuths exhibit increasing residual times with distance, or equivalently a local decrease in phase velocity.

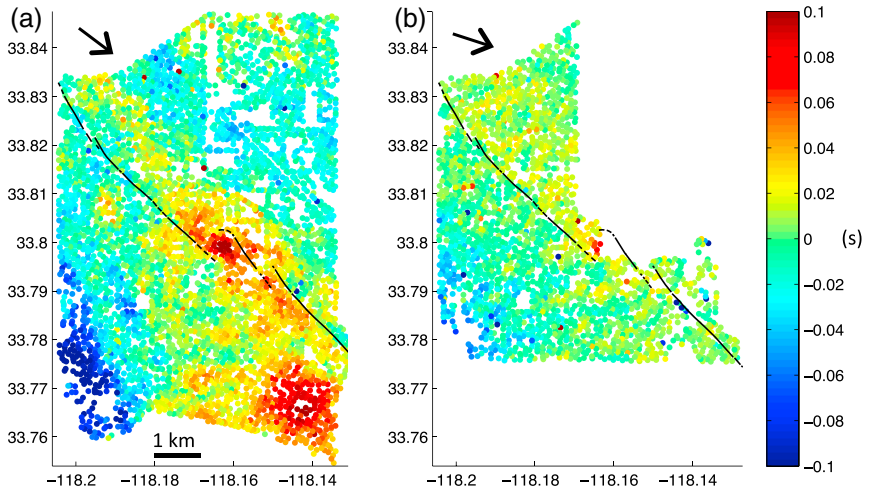

Figure 4. Maps of P residual times for northwest events. Residual time maps for events 1 and 3, which are both from the northwest. Black arrows indicate the azimuth of plane wave propagation.

is ≤0.1 s or approximately one tenth of the dominant period (Figure 3). For the pair of events from the northwest, the residual times are not strongly correlated with distance from the source, but residual times for the southwest events both show a positive correlation with distance (Figure 3). The observed deviation in *P* wave phase velocity for event 2 is equivalent to the difference in phase velocity between a *P* wave from a source at 85° distance and one from a source at 48°, based on the AK135 model. Such strong distortion of the ~1 Hz teleseismic wavefront must occur near the receiver to prevent wavefront healing [e.g., *Nolet and Dahlen*, 2000]. The anomalous phase velocity of *P* waves from southwest events is investigated with forward modeling in section 5. The focus for this section is on observations of lateral heterogeneity within the array.

[11] Maps of P residual times show laterally coherent variations within the Long Beach array for all four events (Figures 4 and 5). To facilitate comparison between southwest and northwest events, the residual time maps for events 2 and 4 are shown with and without a linear distance trend removed from the residual time pattern (Figure 5). Considering that velocity structure is sampled by an ~1 Hz *P* wave, it is impressive that residual time anomalies are observed over lateral distances as short as about 400 m. Locally delayed arrivals are observed near Signal Hill, which is the highest part of the Long Beach anticline and sits between two en echelon branches of the NIFZ [*Wright*, 1991]. Delayed travel times are observed near Signal Hill for all four events. The Signal Hill travel time anomaly is most sharply defined by the residuals for event 2, likely because this event's *P* wave allowed a slightly higher frequency band (up to 1.5 Hz rather than 1.2 Hz) to be used for residual time measurement (Figures 5a and 5b). Where overlapping sampling exists, the maps are generally consistent with each other, though the magnitude of the residual time anomalies such as the Signal Hill anomaly varies. Similarly, a residual time contrast following the northern half of the NIFZ is most clearly exhibited in the map for event 4 (Figures 5c and 5d), and weakly defined for the other events.

[12] Event 1 provides the most complete coverage and is the only event to sample the southernmost quarter of the Long Beach array (Figure 4a). The southwest corner contains an area of early arrivals that is about 3 – 4 km long in the north-northwest direction and about 1.5 km wide. This anomaly abuts the edge of the Long Beach array so its true extent is unknown. The southeast corner contains a nearly circular area of delayed arrivals with a diameter of about 2 km that also abuts the edges of the array. In the scatterplot of Figure 3a, these two regions account for the concentration of negative residual times near the middle of the distance range and the concentration of positive residual times near maximum of the distance range, respectively.

[13] Figure 6 compares mapped residual times for event 1 with time corrections for topography and vertically averaged shear velocity (V_S) in the upper 800 m from a Rayleigh wave tomography model. To obtain a continuous map, the residual times are smoothed onto a 0.01° grid by taking the median value in a cap with a radius of 250 m at each grid point (Figure 6a). We use the median to minimize the influence of spurious travel time measurements that may result from subtle noise-induced distortion of the *P* wave, which can have a large effect because the residuals we measure are a small fraction of the dominant period. Corrections for topography only have a noticeable effect on the residual time map near Signal Hill, which stands at 100 m elevation and is by far the largest topographic feature in the array (Figures 6a–6c). To calculate the topographic correction times, we use the mean shear velocity in the upper 800 m determined by the Rayleigh wave tomography of *Lin et al*. [2013] and assume a corresponding sedimentary V_P/V_S of 2.5 [*Brocher*, 2005].

[14] The *P* wave residual time map for event 1 and the integrated V_S in the upper 800 m are not strongly correlated (Figure 6). The linear correlation coefficient between the maps is 0.26, which is weak and opposite the sign of correlation expected if velocity structure in the upper 800 m dominantly determines *P* wave residual times. The clearest example of positive correlation between the *P* wave residual times and upper 800 m V_S is in the southwest corner of the array, which contains the earliest *P* wave arrivals and among the slowest V_S in the array. Similarly, *P* wave residuals are generally positive in the NIFZ near Signal Hill and V_S is generally high in the same area. The only anomalous area

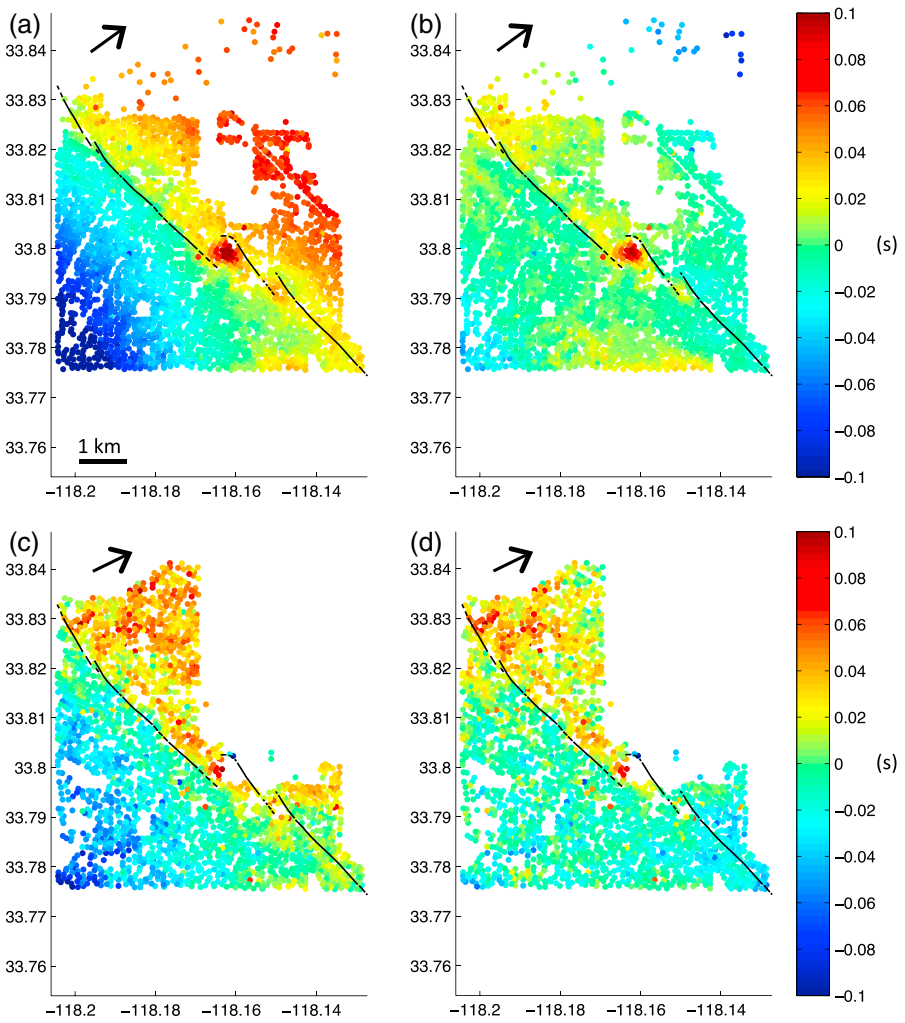

Figure 5. Maps of P residual times for southwest events. Both events 2 and 4 are from southwestern azimuths and exhibit increasing P residual times with distance. The raw residual times for events 2 and 4 are shown in Figures 5a and 5c, respectively. Residual times for events 2 and 4 with a linear distance trend removed are shown in Figures 5b and 5d, respectively. Black arrows in the upper left of each panel indicate the azimuth of plane wave propagation.

where the maps exhibit a negative correlation is in the southeast corner of the array, where the circular area of delayed *P* wave arrivals partially overlaps with an area of low V_S. The generally weak correlation suggests structure deeper than 800 m has a dominant effect on *P* wave residual times because V_P and V_S are positively correlated in dry and water-saturated clastic sedimentary rocks [*Castagna et al.*, 1985], which comprise the upper 800 m beneath the array.

4. *P* Wave Amplitudes

[15] *P* wave amplitudes are analyzed by measuring mean power spectral density (PSD) between 0.4 and 1.2 Hz for all the traces that were accepted for measurement of travel time residuals. For the two deep focus events, the *P* wave was temporally separated from source-side surface reflections (e.g., pP). For the large magnitude (Mw ≥6.9) shallow focus events, it was unavoidable to include source-side surface reflections and the direct *P* wave in the same time window. PSD was estimated using the multitaper method [*Thomson*, 1982], and the mean value between 0.4 and 1.2 Hz at each station is shown in Figure 7. Mean power level across all stations is greatest for event 2, which is a particularly short duration deep focus event. Amplitude maps for all four events exhibit spatially coherent amplitude variations within the Long Beach array.

[16] High amplitudes that are correlated with positive travel time delays are observed near Signal Hill and in the southeast corner of the array. The correlation between positive residual times and high amplitudes suggests elastic focusing by lateral velocity variations as a probable contributor to the amplitude anomalies in these locations. For event 1, which samples the entire array, the correlation between the smoothed residual time (Figure 6c) and amplitude (Figure 8) maps is 0.51. The main area where the residual time and amplitude maps for event 1 are not well correlated is in the northeast corner of the array where we find the lowest amplitudes but near average residual times.

[17] The amplitude map for event 2 shows a beating pattern, with alternating high and low amplitude bands that

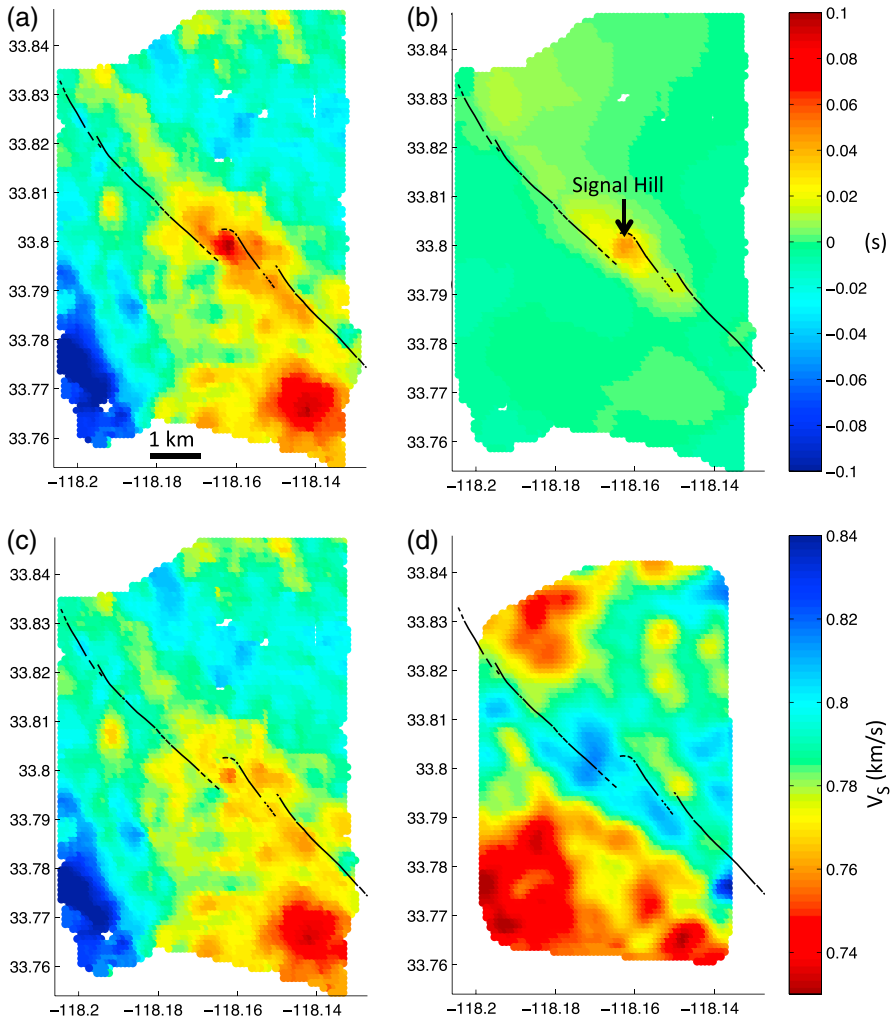

Figure 6. Comparison of P residual times, topographic corrections, and Rayleigh wave tomography. (a) P residual times for event 1, smoothed by taking the median value in a cap with a radius of 250 m. The color-scale is identical for Figures 6a–6c and corresponds to time in seconds. (b) Time corrections for topography. The most prominent feature is Signal Hill. (c) P residual times after correction for topography. (d) Vertically averaged Vs in the upper 800 m from the Rayleigh wave tomography model of *Lin et al.* [2013].

are orthogonal to the propagation direction and only observed in the middle of the array's distance range (Figure 7c). A similar but weaker pattern is observed for event 4 (Figure 7d). This beating pattern suggests the possibility of a secondary arrival that interferes with the *P* wave on account of a different phase velocity (angle of incidence) but similar azimuth. Along with the anomalous *P* wave phase velocity for southwest events it is a further indication that strong lateral heterogeneity exists in a narrow corridor southwest of the Long Beach array. Identification of scattered phases created by the direct *P* wave is the focus of section 5.

5. Vertical Component Receiver Functions

[18] We explore the potential for teleseismic scattered wave imaging with the Long Beach data by using array deconvolution to calculate vertical component receiver functions [*Langston and Hammer*, 2001; *Li and Nabelek*, 1999]. In our approach, the mean signal (in the frequency domain) of all vertical component seismograms for an event is deconvolved from each trace to yield a vertical component receiver function. We use spectral division with a water level to perform the deconvolution [*Helmberger and Wiggins*, 1971; *Clayton and Wiggins*, 1976]. Because only large magnitude earthquakes are well recorded by the Long Beach array, the direct *P* wave temporally overlaps with most scattered arrivals from lithospheric structure. Consequently, the array deconvolution approach can only isolate scattered phases that either have a different phase velocity than the direct *P* wave or are not continuous across the entire array. Hence, scattered waves that are continuous across the entire array and have a phase velocity similar to the direct *P* wave will be removed by deconvolution. In circumstances where smaller magnitude (~ M 5 – 6) teleseismic events are well recorded, the *P* wave signal often is temporally isolated from scattered arrivals of interest (e.g., sediment-basement contact or Moho). In that circumstance, it is possible to use vertical component seismograms to isolate scattered phases that

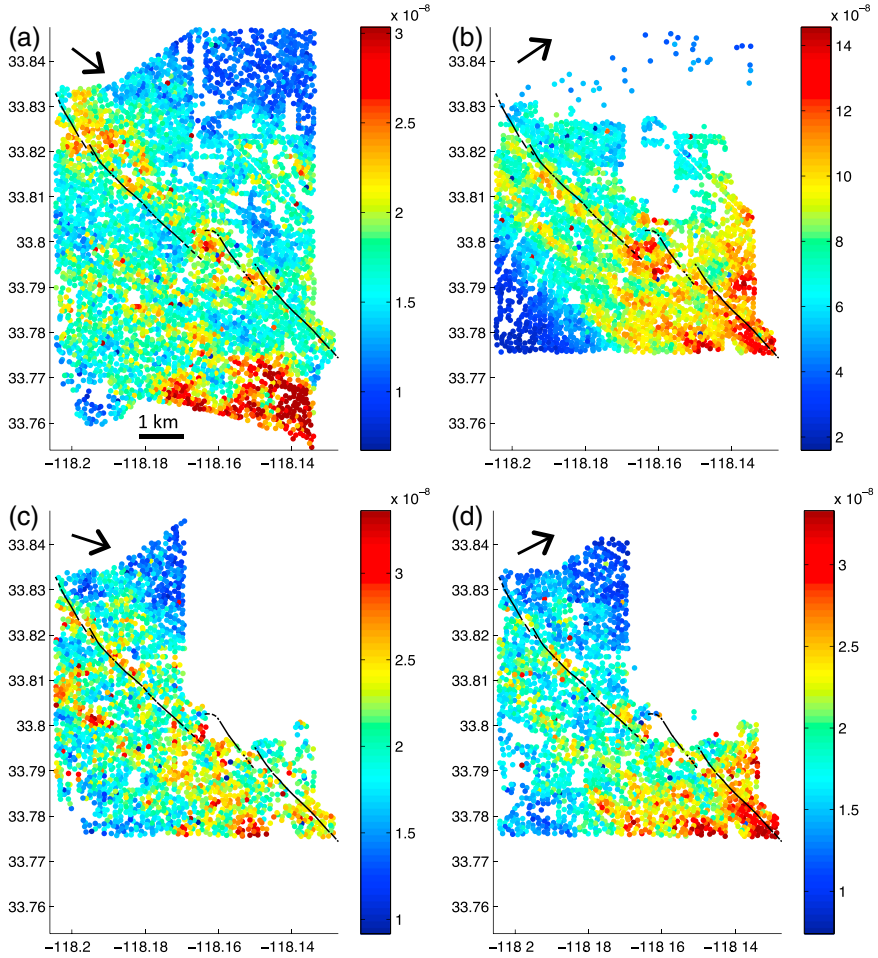

Figure 7. Mean power spectral density between 0.4 and 1.2 Hz. Maps of power spectral density for events 1 – 4 are shown in Figures 7a–7d, respectively. Note that the amplitude color-scale varies for each event. The azimuth of *P* wave propagation is indicated by the black arrow in the upper left of each panel.

arrive after the source function ends regardless of their phase velocity and continuity across the array. Examples include *P* wave reflections from a flat segment of the Moho in southern India [*Tseng et al*., 2006] and from the top of a high-velocity limestone unit in basins adjacent to the Bighorn Mountains in Wyoming [*Yang et al*., 2012].

[19] Figure 9 illustrates the key steps of vertical receiver function analysis for event 2, with data presented in the time domain. The seismograms are aligned using the residual times measured by cross correlation in section 2 (Figure 9a), but for deconvolution we substitute seismograms with greater bandwidth (0.2 – 2 Hz). A time domain example of the array's mean signal is shown in Figure 9b. Deconvolution of the mean signal from each seismogram yields the vertical component receiver functions, which are sorted by distance in Figure 9c. Sorting by distance is motivated by awareness that scattered arrivals with phase velocity similar to the *P* wave are not isolated with this method. The most prominent features of the vertical component receiver functions from event 2 are two positive arrivals with a phase velocity of about 5 km/s, and lag times of 2.8 – 5.5 s (Figure 9c). Note that in the figures the traces are aligned relative to the direct *P* wave and its phase velocity is taken into account to estimate the absolute phase velocity of the scattered arrivals.

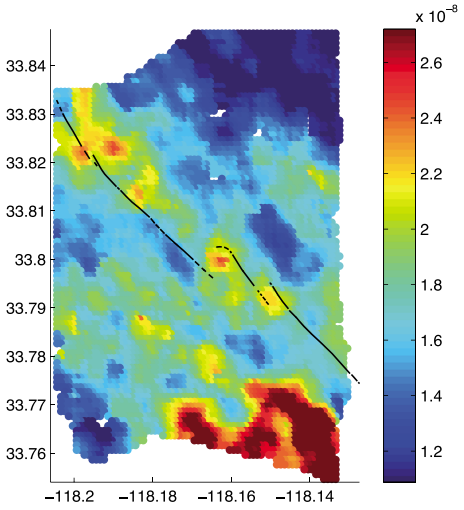

Figure 8. Smoothed amplitude map for event 1. Amplitudes from Figure 7a were smoothed by taking the median in a cap with a radius of 250 m at every point on a 0.01° grid. Relatively high amplitude areas are generally correlated with the positive residual times shown in Figures 6a and 6c.

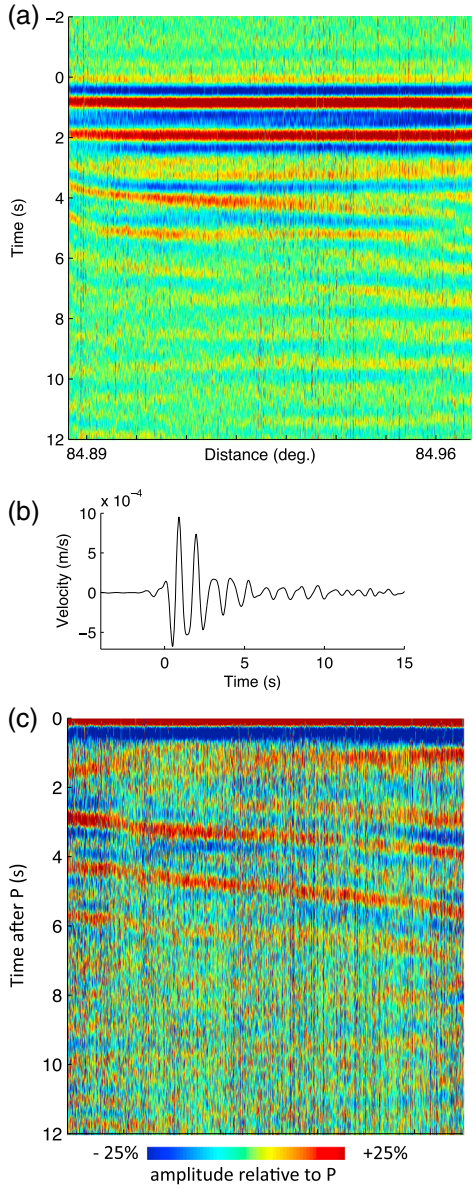

Figure 9. Vertical component receiver function analysis for event 2. (a) Event 2 seismograms aligned by cross correlation and sorted by distance. (b) Stack of the aligned traces. (c) Vertical component receiver functions, which result from deconvolving the stacked trace from each trace in Figure 9a. The positive phases that are coherent across most of the distance range have phase velocities of about 5 km/s.

[20] The other three events produced relatively noisy vertical component receiver functions characterized by ringing. To enhance potential scattered phases in these vertical component receiver functions and facilitate comparison, we stack them in 200 m wide distance bins that are 50% overlapping (Figure 10). The northwest events show a common arrival at 6 – 7 s, which has a phase velocity of about 7.5 km/s. Other arrivals are well defined for event 1 during the first 2 s and in the northwestern half of the array, but unlike the 6 – 7 s arrival these are not consistently observed for event 3. As expected, the stacked image for event 2 better isolates the two strong arrivals that are apparent in Figure 9c. Near the maximum end of the distance range for event 2, the stacked image is characterized by ringing on account of low station density in the northeastern part of the array at that time (Figures 5a and 5b). The presence of two phases that arrive just behind the *P* wave arrival for event 2 and with a different phase velocity is consistent with the beating pattern observed in the amplitude map (Figure 7b). The vertical component receiver functions for event 4 show strong ringing even when stacked in distance bins so they have limited utility for confirming the arrivals in the event 2 receiver functions. There is some consistency between the positive arrivals with about 5 km/s phase velocities in the event 2 receiver functions and the event 4 receiver functions, but for event 4 these phases are not as coherent across the distance range and many other phases with similarly large amplitudes are present.

[21] The phase velocity, polarity, and lag times of the two positive arrivals in the event 2 receiver functions place constraints on their origin. The arrivals cannot be P-to-Rayleigh conversions from topography or strong velocity heterogeneity near the surface [e.g., *Bannister et al*., 1990; *Gupta et al*., 1990; *Clouser and Langston*, 1995] because Rayleigh wave velocity at frequencies near 1 Hz is <1 km/s in the Long Beach array [*Lin et al*., 2013]. Other vertical component receiver function studies isolated *P* waves that reflected at the surface and again at an abrupt interface at depth before arriving at the receiver (PpP_Dp), and these are sometimes referred to as virtual reflections because they can be used similarly to *P* waves created by controlled sources within an array. For reflection from a positive impedance contrast at depth negative polarity PpP_Dp arrivals are expected in vertical receiver functions and have been robustly detected in several settings [e.g., *Li and Nabelek*, 1999; *Bostock*, 2004; *Tseng and Chen*, 2006; *Mercier et al*., 2006; *Yang et al*., 2012]. Here, the strongest phases we isolate are positive. If these are PpP_Dp phases they must originate from negative impedance contrasts at depths of about 9 – 18 km. While it is conceivable that negative impedance contrasts exist, it would be unusual to only detect negative contrasts despite the fact that velocity generally increases with depth.

[22] Rather than the arrivals in the vertical receiver functions being P reflections, it is possible that they are P-to-s conversions (Ps). Steeply dipping interfaces can create Ps conversions that have a different phase velocity than the *P* wave. Using radial receiver functions from an array with ~2 km aperture in the foothills of the Kopet Dagh mountains in Turkmenistan, *Abers* [1998] identified Ps arrivals with a phase velocity of ~3 km/s. He used an inversion of receiver functions from 29 teleseismic events to determine that the origin of the phases was closely correlated with faults that separate the Kopet Dagh mountains from a 10 – 18 km deep sedimentary basin. Here we have useful receiver functions from only three events so we did not conduct similar array processing. However, the results from *Abers* [1998] underscore the possibility that dipping velocity discontinuities can produce Ps phases with substantially different phase velocity than teleseismic *P* waves (13 – 22 km/s). Additionally, Ps phases generated at steeply dipping interfaces are likely to have significant amplitude in vertical component data such as we use here. Forward modeling of the Long Beach travel time residuals presented in section 6 provides

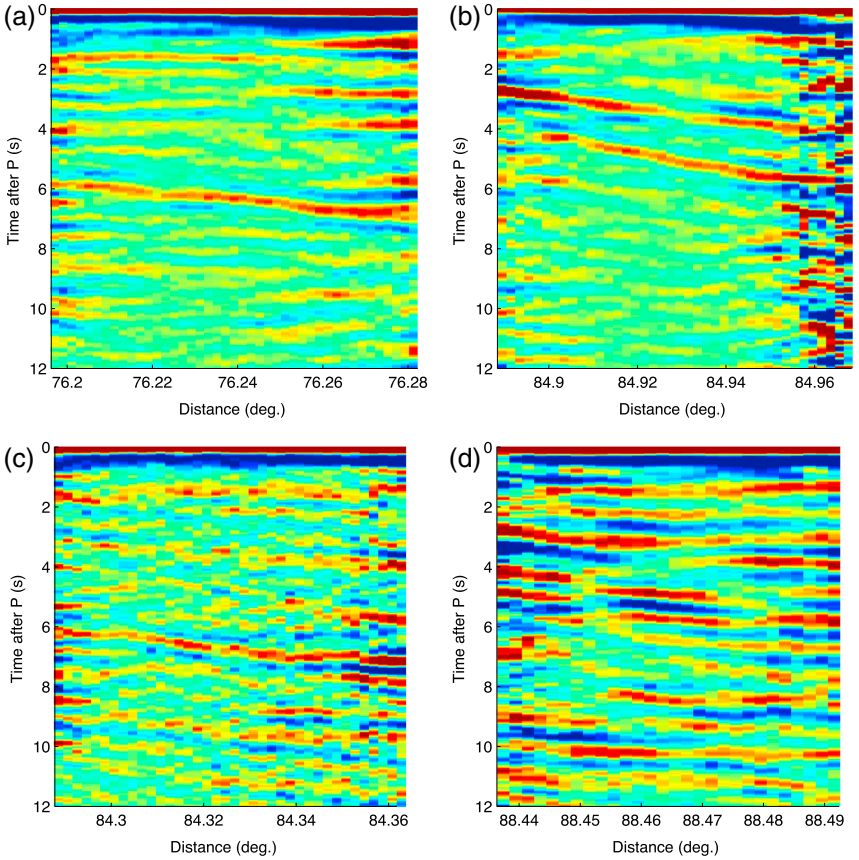

Figure 10. Vertical component receiver functions stacked by distance. The receiver functions for events 1 – 4 are stacked by distance and shown in Figures 10a–10c, respectively. Stacking bins are 200 m wide and 50% overlapping.

complementary insight into the origin of scattered arrivals from the southwest events.

6. 2-D Forward Modeling

6.1. Northeast Dipping Moho Hypothesis

[23] Forward modeling experiments are focused on fitting the anomalous *P* wave phase velocity observed for the two southwest events because it is a simple constraint that requires a large lateral velocity contrast southwest of the array. If upper crustal heterogeneity, such as a gradient in sediment thickness, caused the anomalous phase velocity for southwest events then the P residual time maps for the northwest events would be expected to exhibit a positive trend toward the northeast. The fact that such a trend is not observed for the northwest events rules out a completely upper crustal origin (Figures 4 and 6). It further implies that the lateral velocity contrast responsible for the anomalous *P* wave phase velocity is located southwest of the Long Beach array and sufficiently deep that teleseismic P raypaths from southwest and northwest events sample distinct structure. Owing to the small aperture of the Long Beach array, raypaths from southwest and northwest events diverge completely by 25 km depth (Figure 11), assuming a regional 1-D velocity model [*Hadley and Kanamori*, 1977; *Wald et al*., 1995] and the observed phase velocities. Under the same assumptions, less than one third of the raypath footprints overlap for southwest and northwest events at 15 km depth. Thus, lateral variations in velocity structure at least as deep as the middle-to-lower crust are necessary.

[24] We specifically test the hypothesis that a positive gradient in Moho depth from the Inner Borderland to Long Beach causes the anomalous decrease in *P* wave phase velocity for southwest events. The primary motivation is that prior seismic imaging [*ten Brink et al*., 2000; *Nazareth and Clayton*, 2003; *Zhu and Kanamori*, 2000; *Yan and Clayton*, 2007a; *Richards-Dinger and Shearer*, 1997] and gravity inversions [*ten Brink et al*., 2000; *Miller*, 2002] indicate a positive northeastward gradient in crust thickness near this tectonic boundary and regional-scale tomography models do not image an abrupt change in upper mantle velocities [e.g., *Yang and Forsyth*, 2006; *Schmandt and Humphreys*, 2010]. A secondary motivation for focusing on Moho topography is accumulation of 0.18 s of deviation from the reference moveout over a distance of only 7 km for event 2. This requires a sharp and large magnitude lateral velocity contrast because the 0.4 – 1.5 Hz waveforms used for travel time measurement imply a minimum wavelength of about 5 km in the uppermost mantle. The Moho is typically the strongest velocity contrast at depths below the middle crust so it is likely that Moho topography is the dominant cause of wavefront distortion in this setting. In reality, contributions from lateral heterogeneity within the lower crust and uppermost mantle likely accompany rapid changes in Moho depth, but we use a model with 2 uniform layers (crust and mantle) for simplicity.

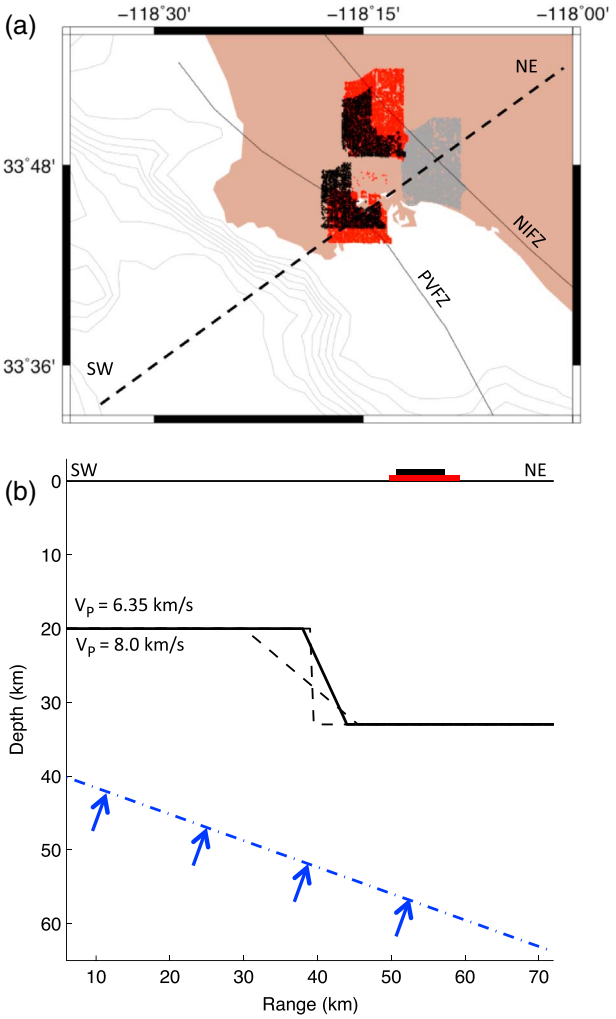

Figure 11. Setup of 2-D models with a linear Moho gradient. (a) Long Beach array stations for event 1 are shown in gray. Ray positions at 25 km depth are shown in red for events 1 and 2 and in black for events 3 and 4. The Newport-Inglewood and Palos Verde fault zones are labeled with thin black lines. (b) Cross-section view of the model with Moho dip of 65° is shown with a solid black line and Moho dips of 40° and 90° are shown with dashed black lines. The surface extent of stations for events 2 and 4 are indicated by the thick red and black lines, respectively. An incident teleseismic *P* wave is indicated by the dashed blue line and blue arrows.

[25] The northeastward increase in Moho depth from the Inner Borderland was parameterized as a linear gradient with a flat Moho on either side (Figure 11). Dip of the Moho gradient and the total increase in crust thickness were varied to optimize the fit to travel time data from events 2 and 4. Inner Borderland Moho depth was set to 20 km because station FMP has robust H-k stacking groups that constrain the Moho to be 20–21 km just offshore of the southwest corner of the Palos Verde peninsula [*Yan and Clayton*, 2007a]. Also, a similar Moho depth of 19 – 20 km was found by offshore reflection imaging northeast of the Catalina Ridge [*ten Brink et al.*, 2000]. Average crustal velocity was set to 6.35 km/s based on a regional 1-D model [*Hadley and Kanamori*, 1977; *Wald et al.*, 1995]. In forward models, the dip of the Moho gradient varied from 20 to 90°, and the depth at which the Moho flattened beneath the mainland varied from 24 to 36 km. The 2-D models assumed that the back azimuth of event 2 is orthogonal to the strike of the Moho gradient. The dip of the gradient was reduced in synthetics for event 4 because its back azimuth is 10° greater than that of event 2. Correction for event 4 obliquity changed the dip by <5° for models that can explain the travel times. If the back azimuth of event 2 is actually oblique to the true gradient, then the forward models provide a slight underestimate of the gradient steepness.

6.2. Forward Model Calculation

[26] Synthetic seismogram calculation was carried out with a 2-D implementation of the staggered-grid finite differences method for elastic wave propagation [*Graves*, 1996]. This approach was chosen because we seek an accurate representation of finite-frequency wavefront healing. Additionally, elastic forward models allow comparison of scattered phases in synthetic and observational data [e.g., *Yan and Clayton*, 2007b]. The synthetic calculations used a time step of 0.01 s and grid spacing of 125 m. A plane wave source with a dominant frequency 1.5 Hz was initiated at the bottom of a rectangular model domain with a width of 400 km and depth of 100 km. The Moho gradient was placed in the middle of the model domain to avoid any artificial reflections not completely eliminated by an attenuating perimeter on the sides and bottom of the model. Synthetic seismometers were placed across a 30 km distance range so that the optimal lateral position for the 6.9 – 9.5 km aperture of the Long Beach array for the two southwest events could be determined for each simulation. Phase velocity of the plane wave was set according to the AK135 model for the source distances of events 2 and 4. For travel time measurements, the synthetic waveforms were corrected for short-period instrument response and then filtered to the same frequency band used for the observational data. Alignment of the waveforms by multichannel cross correlation [*VanDecar and Crosson*, 1990] was used to determine travel time residuals within the synthetic array aperture. Examples of model fit to the observational travel time data are shown in Figure 12.

6.3. Forward Modeling Results

[27] To illustrate the constraints provided by forward modeling the synthetic travel time residuals are overlaid on the observational residuals for three models with a 13 km increase in crust thickness and Moho dips of 40°, 65°, and 90°, respectively [Figure 12]. There are clear variations in how well the different models fit the trend of observed travel time residuals for event 2. Event 4 provides weaker constraint on account of narrower aperture and greater scatter in residual times. Because the incident wavelength near the Moho is about 5 km, greater recording aperture for event 2 (9.5 km) provides a substantial increase in constraint on velocity structure. The 40° model does not match the steep residual time trend near the minimum of the distance range for event 2 (Figure 12c), and the 90° model results in too tight a kink in the residual time trend (Figure 12e). The slightly arcuate positive trend in residual times is well fit by the 65° model. The two layer forward modeling results show that it is possible to fit the trend in residual times by only

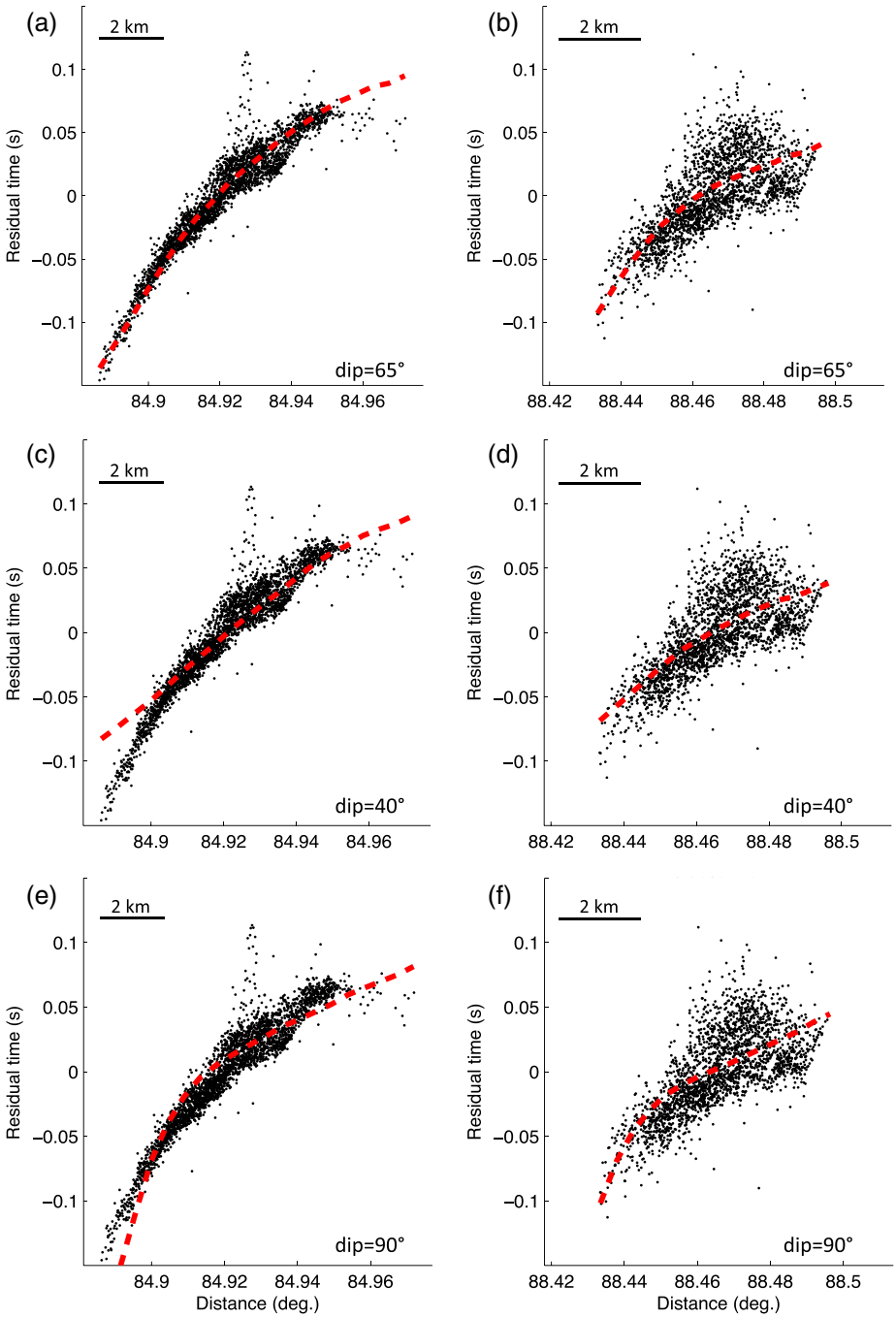

Figure 12. Synthetic model fits to P residual times for southwest events. Synthetic P residual times (red dashed) for models with the Moho dipping northeast at (a,b) 65°, (c,d) 40°, and (e,f) 90° are overlaid on the observed residual times.

introducing a linear gradient in thickness of the continental crust, and the best fit to the data was obtained for a model with 13 km increase in Moho depth and 65° dip.

[28] An undesirable aspect of this model structure is that it clearly conflicts with estimates of Moho depth near the Los Angeles Basin. The PmP stacking analysis of *Richards-Dinger and Shearer* [1997] finds a Moho depth of ~26 km near the Los Angeles basin. However, it is notable that the strongest gradient in their regional crust thickness map is located near Long Beach and their results are inherently smooth because they stacked PmP reflection points in 0.25° bins. Another relevant aspect of the PmP stacking analysis of *Richards-Dinger and Shearer* [1997] is that the leading edge of stacked energy with a moveout consistent with PmP is used to determine crustal thickness. If multiple discontinuities exist near the base of the crust then the shallowest interface could be designated as the Moho. Regional maps of crust thickness have also been made using receiver functions. These studies have avoided stations in basins so there is a gap in their results landward of the

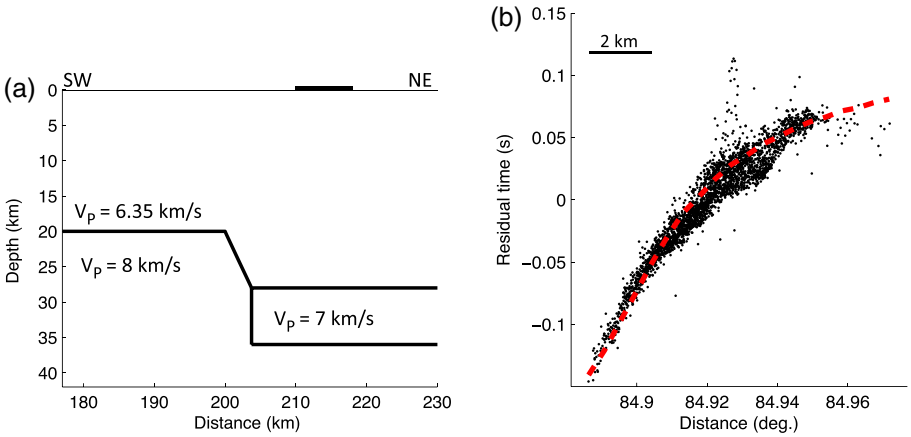

Figure 13. Forward modeling with an intermediate velocity layer. (a) Two-dimensional model with a 65° Moho dip and an 8 km thick intermediate velocity layer beneath the felsic crust northeast of the gradient. The increase in felsic crust thickness is from 20 to 28 km. (b) Comparison of event 2 residual times with residual times from synthetic seismograms for the model with an intermediate velocity layer.

Palos Verde peninsula, but even farther inboard on the north and east sides of the Los Angeles basin estimates of Moho depth from receiver functions are about 28 – 30 km [*Yan and Clayton*, 2007a]. In light of these constraints, we tested an alternative model that includes contributions from lateral heterogeneity aside from Moho topography.

[29] We constructed an alternative model by adding a layer of intermediate velocity beneath the felsic continental crust layer (the 6.35 km/s layer) on the inboard side of the Moho gradient. The goal of this modification is to find a simple model that can also fit the residual times, but without requiring unreasonable thickness of felsic continental crust at the southwest edge of the Los Angeles basin. In general, a northeastward decrease in velocity at lower crust or uppermost mantle depths is needed to create the observed effect on teleseismic P travel times from the southwest. A simple modification to reduce velocity on the northeast side of the Moho gradient is to add a layer with intermediate velocity (V_P = 7 km/s). We choose to modify the northeast side of the gradient because on southwest side the *P* waves are primarily sensitive to the uppermost mantle and velocity there is unlikely to be much greater than 8 km/s [*Nazareth and Clayton*, 2003; *Buehler and Shearer*, 2012]. Addition of an 8 km thick layer with V_P = 7 km/s beneath the felsic or V_P = 6.35 km/s portion of the crust inboard of the Moho gradient allows an 8 km increase in crust thickness (still with a 65° dip) to provide a good fit to the travel time pattern observed for event 2 (Figure 13). The model in Figure 13 contains a vertical truncation of the intermediate velocity layer. Tests that extended the 65° dip across the edge of the intermediate velocity layer provided a poorer fit to the residual time trend for event 2.

[30] The idealistic models tested here demonstrate that an abrupt lateral transition is needed, though we cannot

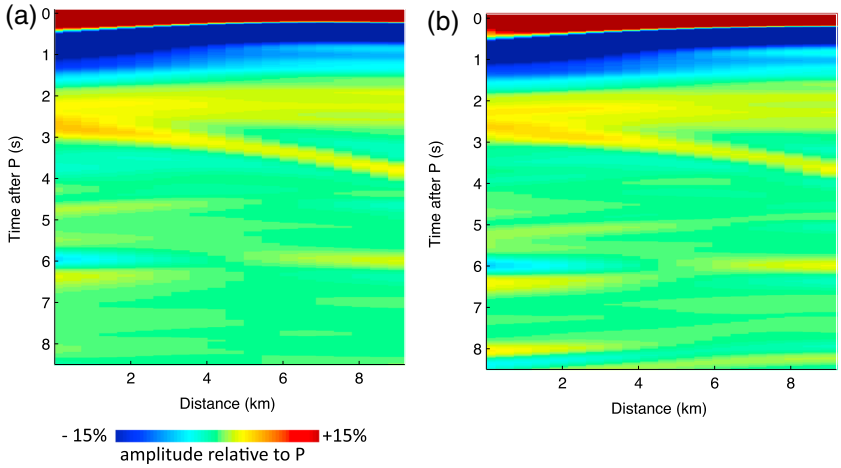

Figure 14. Synthetic vertical component receiver functions for models with and without an intermediate velocity layer. (a) Synthetic vertical receiver functions for the 65° Moho dip model with an increase in felsic crust thickness from 20 to 33 km (Figure 11). (b) Synthetic receiver functions for the model with 65° Moho dip, felsic crust thickness increase from 20 to 28 km, and an intermediate velocity layer beneath the felsic crust northeast of the gradient (Figure 13). Note that subhorizontal interfaces are not well imaged with vertical component receiver functions in this narrow aperture array.

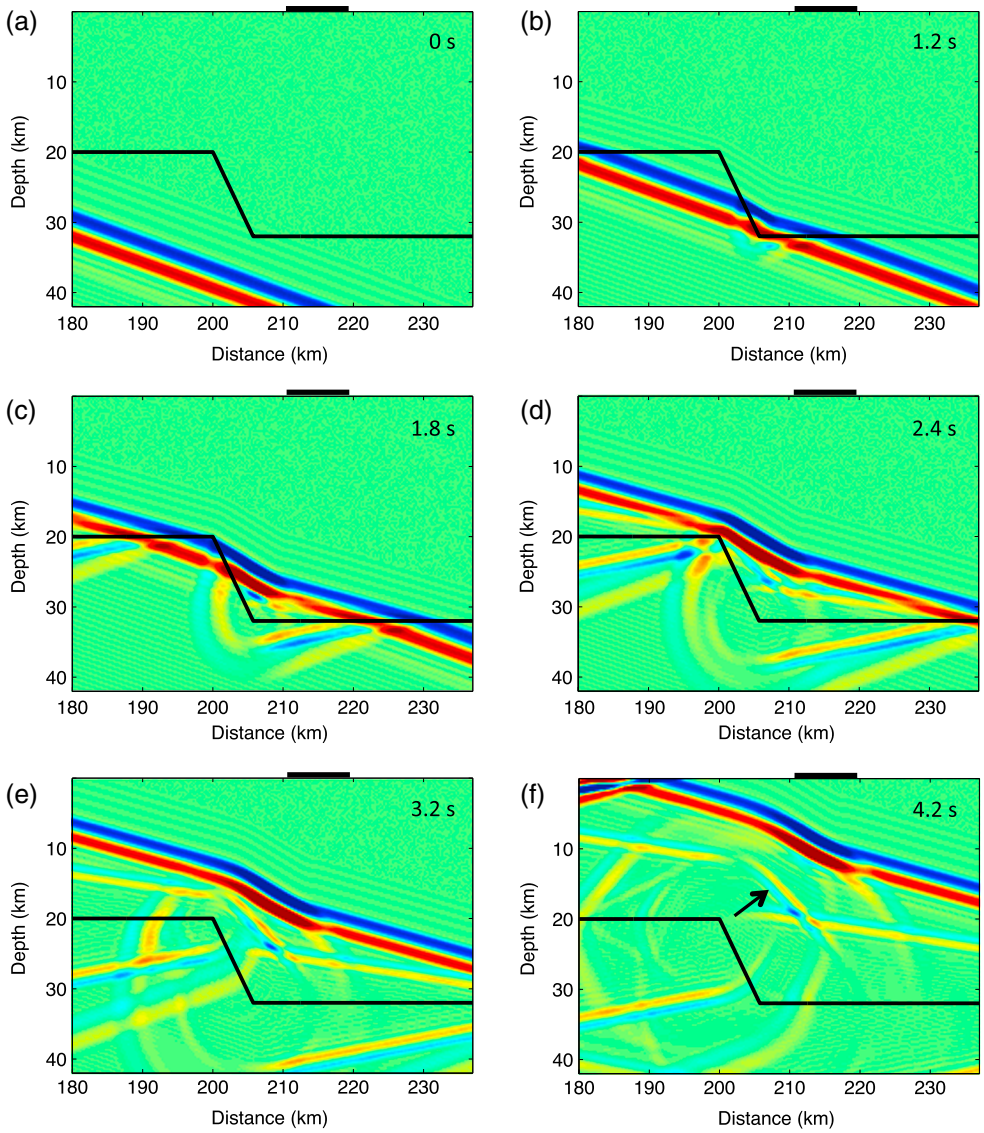

Figure 15. Snapshots of the wavefield from an elastic simulation. The time in the upper right corner of each panel is given relative to the time in Figure 15a. Hypothetical location of the Long Beach array is labeled by the solid black line at the surface. The sequence of snapshots shows the *P* wave interaction with the Moho that includes a segment with a 65° dip. Note the increasing separation between the *P* wave and the steeply dipping phase labeled with a black arrow. This secondary arrival is a Ps conversion from the dipping Moho, which arrives at the array with a phase velocity of 5.4 km/s.

uniquely constrain how the lateral velocity contrast is partitioned between Moho topography and other lateral variations in lower crust and uppermost mantle structure, such as introduction of an intermediate velocity layer. The most robust result is that the lateral change in velocity structure is located at about 20 – 35 km depth and occurs over about 3.75 – 6 km laterally. To further test the simple models that fit the travel times and address whether or not a steeply dipping discontinuity is required by the data, we calculated synthetic vertical component receiver functions for these models.

6.4. Vertical Receiver Functions From Forward Models

[31] Vertical receiver functions were calculated with synthetic data following the same processing described for the observational data in section 5. The resulting receiver functions are arranged by distance and compared with the event 2 receiver functions stacked in distance bins (Figure 14). Both models with a 65° Moho dip yield synthetic vertical receiver functions that have a positive arrival with phase velocity of about 5 km/s and lag time ranging from about 2.7 to 3.8 s. The amplitude of this arrival is greater near the minimum end of the distance range. These characteristics are remarkably similar to those of the first prominent arrival in the event 2 receiver functions (Figure 10), with the exception of relatively low amplitude for the later arriving phases in the synthetics. Also, the phase velocity of the synthetic arrival is 5.4 km/s and the phase velocity of the observed arrival is 4.7 km/s. The origin of the phase in the synthetics is a Ps conversion from the steep Moho gradient. In snapshots of the wavefield from

an elastic simulation, the rate of separation between the direct *P* wave and the steeply dipping phase marked with an arrow clearly identifies it as an *S* wave (Figures 15e and 15f). The simulation shown in Figure 15 uses a model without an intermediate velocity layer so that it is easier to identify the conversion from the steep Moho gradient. As shown in Figure 14, the vertical component receiver functions contain a prominent Ps conversion from the dipping interface regardless of whether or not an intermediate velocity layer is added beneath the layer with $V_P = 6.35$ km/s. A basic result of our forward modeling experiments is that Ps conversions can create prominent arrivals in vertical receiver function in locations where steeply dipping interfaces are present.

[32] The synthetics do not provide an explanation for the second prominent arrival in the event 2 receiver functions. There are multiple possible origins for the second arrival. It is potentially another Ps conversion either from an interface that is deeper and farther southwest, or from out-of-plane variations in the same interface that creates the earlier arrival. If it originates from a separate deeper interface, the ~1.5 s difference in lag time between the two phases would imply a sub-parallel deeper interface with a separation of about 12 – 16 km. The increase in path length from interface to the Long Beach array would have to be similar if it is due to out-of-plane variations. As a result of the relatively noisy receiver functions for event 4, we lack strong confirmation that the positive arrivals in the event 2 receiver functions would be similarly isolated from waveforms of different earthquake sources. With a greater number of events, an inverse problem could be posed to constrain the origin of the second phase in the event 2 receiver functions [e.g., *Abers*, 1998], and determine whether or not an interface exists in the lithospheric mantle.

7. Discussion

7.1. Upper Crustal Structure

[33] Advances or delays in teleseismic *P* wave travel times within the Long Beach array are indicative of heterogeneous velocity structure in the upper crust, but the specific depth and magnitude of velocity heterogeneity are uncertain. One likely influence on the travel times of near-vertically propagating *P* waves is local variations in thickness of sedimentary strata, which could affect travel times as a result of the expected velocity contrast between clastic sediments and metamorphic or igneous basement rocks. In the following discussion, we infer sediment thickness from the depth to the base of the ~14 Ma Mohnian deposits as contoured by *Wright* [1991]. Consistent with the expectation that sediment thickness and P residual times will be positively correlated, we find negative residual times in the southwest corner of the array (Figure 6) coincident with decreasing sedimentary thickness toward the Palos Verde peninsula. Measurements of low amplitudes in the same area also are consistent with expectation of relatively high velocity (Figure 8). However, the actual importance of total sedimentary thickness for our travel time observations is unclear because the delayed travel time anomalies in the southeast corner of the array and in the NIFZ near Signal Hill do not correspond to areas of increased sediment thickness. Additionally, we measure relatively low amplitudes near the northern edge of the array where sediment thickness is greatest. These results imply that factors aside from sediment thickness must have strong influences on the observed travel time and amplitude patterns.

[34] Locally delayed travel times and increased amplitudes at Signal Hill are of particular interest because they occur at the site of an historically productive oil reservoir and the local stratigraphy is constrained by well data [*Wright*, 1991]. Signal Hill forms the crest of the Long Beach anticline, where well data show that basement rocks rise to slightly shallower depths relative to adjacent areas [*Wright*, 1991]. Here travel times are delayed by up 0.12 s and amplitudes are increased despite the local decrease in sedimentary thickness. We estimate a topographic correction with a maximum of 0.05 s at the peak of Signal Hill, so subsurface heterogeneity is required to explain the travel time delays (Figure 6). Further support for the presence of low-velocities beneath Signal Hill is provided by observations of increased amplitudes in the same area. Aside from sediment thickness other factors such as locally increased fracture density [e.g., *Moos and Zoback*, 1983], decreased fluid content in porous rocks [*Castagna et al*., 1985; *Mukerji and Mavko*, 1994], or changes in anisotropy [*Wang*, 2002] must contribute to the observed P travel times and amplitudes.

[35] A prominent anomaly at Signal Hill is not imaged in a Rayleigh wave tomography model of the upper 800 m, which suggests the heterogeneity that dominantly affects the *P* wave measurements is located at greater depth (Figure 6). Coincidence of the travel time and amplitude anomalies with the crest of the Long Beach anticline makes it unlikely that the heterogeneity responsible for these signals lies within the basement rocks. Near this location, wells encounter basement rocks at 3500 – 4500 m. The depth range between the bottom of the Rayleigh-wave model and the basement contains nearly all the productive intervals for petroleum extraction, which are located between 600 and 2300 m [*Wright*, 1991]. Thus, it appears likely that the *P* wave travel time and amplitude anomalies at Signal Hill arise due to structure in the depth range from which oil has been extracted over the past 90 years. Constraints from teleseismic *P* waves smooth over larger lateral distances than active source data, but the different illumination direction and frequency content of teleseismic *P* waves may have utility in characterizing reservoir properties.

7.2. A Locally Abrupt Boundary to Inner Borderland Rifting

[36] The positive trend in travel time residuals with increasing distance for both southwest events requires a strong lateral gradient in velocity structure southwest of the array. Forward modeling experiments show that the positive trend in travel time residuals is consistent with a 65° northeastward Moho dip and change in crust thickness of 8 – 13 km. The idealistic structures shown to fit the data serve as gauges of the lateral sharpness and magnitude of the northeastward change in lithospheric structure. In the models with a 65° Moho dip, the lateral transition occurs over 3.75 – 6 km, with the lower value corresponding to the model with an intermediate velocity layer beneath the felsic continental crust on the inboard side. The fact that models with or without the intermediate velocity layer fit the observed trend in travel time residuals for event 2 demonstrates there is a tradeoff between travel time variations originating from local

Moho topography and from heterogeneity within the lower crust or uppermost mantle. Evidence for an important contribution from a dipping velocity discontinuity comes from the similarity between the ~5 km/s phase in the synthetic and event 2 vertical receiver functions (Figure 14). To explain the travel time and receiver function results, we favor a structural transition that is composed of a steeply dipping northeastward increase in Moho depth combined with lateral heterogeneity within the uppermost mantle or lower crust. An example of such a structure is the model with an intermediate velocity layer beneath the 6.35 km/s layer on the northeast side of the gradient (Figure 13). This model yields a good fit to the observational results for southwest events and avoids the unreasonable crust thickness beneath Long Beach that is predicted by the two-layer model (Figure 11).

[37] Two potential origins for an intermediate velocity layer are basal accretion of former Farallon ocean crust and magmatic underplating during Miocene volcanism. Basal accretion of oceanic crust that stalled during subduction termination and initiation of the transform margin has been suggested along much of the California coast [*Brocher et al*., 1999]. Here, lateral truncation of accreted slab crust beneath the Palos Verde peninsula could have occurred when capture of the Monterey microplate by the Pacific initiated rotation of the western Transverse Ranges block [*Nicholson et al*., 1994]. A slab rupture scenario in response to Monterey capture and western Transverse Ranges rotation was previously suggested by *ten Brink et al*. [1999]. In the context of an oceanic crust origin, the velocity assumed in our model ($V_P = 7$ km/s) is probably too high because mean velocity in ocean crust layer 3 is about 6.75 km/s [*Christensen and Salisbury*, 1975]. A corresponding reduction in thickness of the intermediate layer to 6.5 – 7 km allows a more appropriate ocean crust velocity structure to achieve an equivalent fit to our observational results. A second potential tectonic origin is that after subduction termination the entire lithospheric column of the Farallon slab fell away from the base of the crust in this area and melts resulting from the upwelling return flow ponded and crystallized at the base of the crust. The assumed intermediate velocity in Figure 13, $V_P = 7$ km/s, is consistent with a gabbroic composition [*Christensen and Salisbury*, 1975]. In the Long Beach oilfield and on the Palos Verde peninsula, a transient phase of volcanism, often referred to as slab window volcanism, occurred between 12 and 17 Ma [*Wilson et al*., 2005 and references therein]. The intermediate layer is laterally continuous to the northeast in our models; however, the lateral extent of the hypothetical layer is not constrained because of the extremely local corridor of sampling provided by two similar distance southwest events recorded by a small aperture array.

[38] The most striking result of this study in regard to lithospheric structure is identification of a narrow structural boundary located about 10 – 16 km southwest of the NIFZ at depths of about 20 – 35 km. We consider this feature the local boundary of Inner Borderland rifting at lower crust and uppermost mantle depth. In the upper crust, the NIFZ is often considered the eastern limit of the Inner Borderland near the latitude of Long Beach because granite rather than Catalina schist is found in wells that reach the basement on the northeast side of the NIFZ [*Yerkes et al*., 1965; *Wright*, 1991]. Our analyses of the Long Beach data indicate that the boundary of the Inner Borderland at Moho depth lies southwest of the NIFZ, roughly between the surface trace of the Palos Verde fault and southwest coast of the Palos Verde peninsula. Extension of the Inner Borderland peaked in the Miocene and most right lateral deformation near the Long Beach array is thought to be post Pliocene [e.g., *Bohannon and Geist*, 1998, *Crouch and Suppe*, 1993]. Holocene deformation of the NIFZ and Palos Verde faults is dominated by right-lateral offset. Total right-lateral displacement on both fault zones is debated, but probably only a few km for the NIFZ [*Harding*, 1973; *Campbell and Yerkes*, 1976; *Wright*, 1991; *Crouch and Suppe*, 1993] and ≤10 km for the Palos Verde fault if post-Pliocene or younger slip rates [*Stephenson et al*., 1995; *McNeilan et al*., 1996; *Brankman and Shaw*, 2009] are assumed to be constant since inception as a right lateral fault [*Ward and Valensise*, 1994]. The small magnitude of right-lateral offset subsequent to rifting suggests that the narrow transition in lithospheric structure we identify represents an abrupt boundary to crustal thinning associated with opening of the Inner Borderland rather than juxtaposition of heterogeneous blocks by a large strike-slip offset.

[39] A localized boundary to Inner Borderland rifting near this location was recently suggested based on regional scale imaging with Sp receiver functions calculated for broadband SCSN stations. *Lekic et al*. [2011] imaged a negative velocity gradient suggested to represent the lithosphere-asthenosphere boundary beneath southern California and found that the depth of the seismic interface was about 75 km beneath the Los Angeles basin and decreased to about 45 km depth immediately southwest of the NIFZ. They considered the boundary to be abrupt at the limit of their resolution with about 15 km station spacing and a dominant frequency of about 0.1 Hz. Our results provide additional support for the presence of a narrow boundary and show that, at least locally, the transition in structure may occur over a horizontal distance of <6 km.

[40] The existence of Moho topography as steep as 65° at the edge of the Inner Borderland is at odds with the common expectation of viscous lower crustal flow in locations with core-complex style extension and high heat flow [e.g., *Block and Royden*, 1990]. Creation and maintenance of this localized gradient likely require a rheological contrast that preceded opening of the Inner Borderland, rather than extension of initially uniform lithosphere, which is most often modeled to investigate generic dynamics of rifting [e.g., *Buck*, 1991; *Huismans and Beaumont*, 2003]. We speculate that intermediate velocity layer in our preferred model could be related to preservation of a steep structural transition by introducing a relatively strong basaltic layer just beneath the felsic mainland crust. Owing to the narrow corridor sampled by the Long Beach array, it is uncertain whether this portion of the eastern boundary to the Inner Borderland is anomalously steep or if similar gradients are maintained along strike.

7.3. Potential for High-Resolution Passive Source Imaging

[41] Measurements of travel times and amplitudes of teleseismic *P* waves recorded with mean station spacing of about 120 m demonstrate that typical instrument spacing in passive source arrays (5 – 100 km) is far from recovering

heterogeneity at the fine-scale limit imposed by illumination from teleseismic sources. Features such as the delayed travel times and increased amplitudes at Signal Hill could be entirely missed with instrument spacing of 1 km or subject to biased sampling with station spacing sparser than about 200 m. Our results provide a conservative estimate of what can be achieved with teleseismic earthquakes recorded by dense short period arrays. One reason is that a greater number of earthquakes likely would have produced useful waveforms if not for the survey's use of a filter to reduce the strength of signals below 3 Hz. Tests are being conducted to see if this filter is really necessary for active source recordings. Additionally, future surveys that plan to use teleseismic data could deploy instruments with lower corner frequencies, which would increase the number of high quality events and signal bandwidth. For example, using instruments with 4.5 Hz corner frequency, *Yang et al*. [2012] recorded high quality waveforms for Mb 5.2 – 5.4 teleseismic earthquakes. Aside from changes in recording configuration, the maximum frequency content of teleseismic *P* waves recorded in Long Beach also is limited by the fact that southern California is a region of relatively high attenuation in the upper mantle [*Dalton et al*., 2008; *Hwang et al*., 2011]. In lower attenuation regions, one can expect greater teleseismic bandwidth and illumination of even finer scale heterogeneity than in this study.

[42] More comprehensive seismic imaging methods would be feasible with high quality teleseismic waveforms from a greater range of azimuths and distances. Beneath the array footprint teleseismic waveform tomography methods that use both phase and amplitude information [e.g., *Roecker et al*., 2010] could be applied at new scales to provide detailed constraints on crustal structure. Teleseismic illumination beneath the array could also be sufficient for interferometric methods of *P* wave reflection imaging [*Abe et al*., 2007; *Ruigrok et al*., 2010; *Nowack et al*., 2006]. Scatters that originate beyond the footprint of the array, such as the Ps arrival from the dipping Moho discussed here, may not be adequately illuminated for robust scattered wave image construction. However, it would be possible to place quantitative bounds on the origin of scattering and compare them with complementary constraints on nearby structure [e.g., *Abers*, 1998]. Our results suggest caution in scattered wave imaging with only a narrow range of illumination angles because migration of P reflections could suffer from interference with Ps scattering, or vice versa. Identification of the dominant sources of scattered energy and whether scattered phases are *P* or *S* waves would be more straightforward with three-component data [e.g., *Leahy et al*., 2012], but our analysis shows that there is strong potential for scattered wave imaging of lithospheric discontinuities with only vertical data in narrow aperture arrays (~10 km).

8. Concluding Remarks

[43] We have measured travel times and amplitudes of teleseismic *P* waves recorded by a dense petroleum industry survey with mean station spacing of about 120 m and array aperture of 7 – 10 km. Detection of both travel time and amplitude anomalies that are laterally coherent over length-scales as small as about 400 m indicates teleseismic *P* waves could be a useful complement to active source imaging for studies of upper crustal structure. The travel time data also proved useful for identification of an abrupt boundary in lithospheric structure southwest of the array at lower crust and uppermost mantle depths. Forward modeling showed that the anomalous phase velocity of *P* waves from the southwest is consistent with a 65° Moho dip toward the northeast. Vertical component receiver functions calculated with observational data and synthetic data for a model with a 65° northeastward Moho dip both exhibit a positive arrival with a phase velocity of about 5 km/s. At least locally, this suggests a boundary to Inner Borderland rifting that is much more localized than estimates from previous regional studies. The basic analyses of teleseismic *P* waves we conducted demonstrate that even a few events that are well recorded by dense short period arrays can be a rich source of information. In conjunction with recent work on ambient noise interferometry [*Lin et al*., 2013], our results point toward potential for entirely passive seismic experiments with ability to resolve fine-scale heterogeneity from near surface to upper mantle depths.

[44] **Acknowledgments.** NodalSeismic LLC and Signal Hill Petroleum Inc. are thanked for providing data access, and we specifically thank Dan Hollis for his efforts in making the data available. We thank Craig Jones and Vadim Levin for constructive reviews. This research was supported in part by the Gordon and Betty Moore Foundation through the Tectonics Observatory at Caltech and by NSF grant EAR1214912. This is contribution #237 from the Tectonics Observatory. B.S. was also partially supported by the University of New Mexico.

References

Abe, S., E. Kurashimo, H. Sato, N. Hirata, T. Iwasaki, and T. Kawanaka (2007), Interferometric seismic imaging of crustal structure using scattered teleseismic waves, *Geophys. Res. Lett.*, *34*, L19305, doi:10.1029/2007GL030633.

Abers, G. A. (1998), Array measurements of phases used in receiver-function calculations: importance of scattering, *Bull. Seismol. Soc. Am.*, *88*, 313–318.

Atwater, T., and J. Stock (1998), Pacific-North America plate tectonics of the Neogene southwestern United States—An update, *Int. Geol. Rev.*, *40*, 375–402.

Bannister, S. C., E. S. Husbeye, and B. O. Rudd (1990), Teleseismic P coda analyzed by three-component and array techniques; deterministic location of topographic P-to-Rg scattering near the NORESS array, *Bull. Seismol. Soc. Am.*, *80*, 1969–1986.

Bird, P., and R. W. Rosenstock (1984), Kinematics of present crust and mantle flow in southern California, *Geol. Soc. Am. Bull.*, *95*, 946–957.

Block, L., and L. H. Royden (1990), Core complex geometries and regional scale flow in the lower crust, *Tectonics*, *9*(4), 557–567, doi:10.1029/TC009i004p00557.

Bohannon, R. G., and E. Geist (1998), Upper crustal structure and Neogene tectonic development of the California continental borderland, *Geol. Soc. Am. Bull.*, *110*, 779–800.

Bostock, M. G. (2004), Green's functions, source signatures, and the normalization of teleseismic wave fields, *J. Geophys. Res.*, *109*, B03303, doi:10.1029/2003JB002783.

Brankman, C. M., and J. H. Shaw (2009), Structural geometry and slip of the Palos Verdes fault, southern California: Implications for earthquake hazards, *Bull. Seismol. Soc. Am.*, *99*, 1730–1745.

Brocher, T. (2005), Empirical relations between elastic wavespeeds and density in the Earth's crust, *Bull. Seismol. Soc. Am.*, *95*(6), 2081–2092, doi:10.1785/0120050077.

Brocher, T. M., U. S. ten Brink, and T. Abramovitz (1999), Synthesis of crustal seismic structure and implications for the concept of s slab gap beneath coastal California, *Int. Geol. Rev.*, *41*, 263–274.

Buck, W. R. (1991), Modes of continental lithospheric extension, *J. Geophys. Res.*, *96*(B12), 20,161–20,178.

Buehler, J. S., and P. M. Shearer (2012), Localized imaging of the uppermost mantle with USArray Pn data, *J. Geophys. Res.*, *117*, B09305, doi:10.1029/2012JB009433.

Campbell, R. H., and R. F. Yerkes (1976), Cenozoic evolution of the Los Angeles basin area—Relationship to plate tectonics, in *Aspects of the Geological History of the California Borderland*, edited by D. G.

Howell, Misc. Publ. 24, pp. 541–558, Pac. Sect., Am. Assoc. of Pet. Geol., Bakersfield, Calif.

Castagna, J. P., M. L. Batzle, and R. L. Eastwood (1985), Relationships between compressional-wave and shear-wave velocities in clastic silicate rocks, *Geophysics*, *50*, 571–581.

Christensen, N. I., and M. H. Salisbury (1975), Structure and constitution of the lower oceanic crust, *Rev. Geophys.*, *13*, 57–83.

Clayton, R. W., and R. A. Wiggins (1976), Source shape estimation and deconvolution of teleseismic body waves, *Geophys. J. R. Astron. Soc.*, *47*, 151–177.

Clouser, R. H., and C. A. Langston (1995), Effect of sinusoidal interfaces on teleseismic P-wave receiver functions, *Geophys. J. Int*, *123*, 541–558.

Crouch, J. K., and J. Suppe (1993), Late Cenozoic evolution of the Los Angeles basin and inner California borderland: A model for core complex-like crustal extension, *Geol. Soc. Am. Bull.*, *105*, 1414–1434, 1993.

Dalton, C. A., G. Ekström, and A. M. Dziewonski (2008), The global attenuation structure of the upper mantle, *J. Geophys. Res.*, *113*, B09303, doi:10.1029/2007JB005429.

Ekström, G., M. Nettles, and A. M. Dziewonski (2012), The global CMT project 2004-2010: centroid-moment tensors for 13,017 earthquakes, *Phys. Earth Planet. Inter.*, *200-201*, 1–9.

Graves, R. W. (1996), Simulating seismic wave propagation in 3-D elastic media using staggered-grid finite differences, *Bull. Seismol. Soc. Am.*, *86*, 1091–1106.

Grove, M., and G. E. Bebout (1995), Cretaceous tectonic evolution of coastal southern California: insights from the Catalina Schist, *Tectonics*, *14*, 1290–1308.

Gupta, I. N., C. S. Lynnes, T. W. McElfresh, and R. A. Wagner (1990), F-k analysis of NORESS array and single station data to identify sources of near-receiver and near-source scattering, *Bull. Seismol. Soc. Am.*, *80*, 2227–2241.

Hadley, D., and H. Kanamori (1977), Seismic structure of Transverse Ranges, California, *Geol. Soc. Am. Bull.*, *88*(10), 1469–1478.

Harding, T. P. (1973), Newport-Inglewood trend, California—An example of wrenching style of deformation, *Am. Assoc. Pet. Geol. Bull.*, *57*, 97–116.

Hauksson, E. (1987), Seismotectonics of the Newport-Inglewood fault zone in the Los Angeles basin, southern California, *Bull. Seismol. Soc. Am.*, *77*, 539–561.

Hauksson, E., and S. Gross (1991), Source parameters of the 1933 Long Beach earthquake, *Bull. Seismol. Soc. Am.*, *81*, 81–98.

Helmberger, D. V., and R. Wiggins (1971), Upper mantle structure of mid-western United States, *J. Geophys. Res.*, *76*(14), 3229–3245.

Hornafius, J. S., B. P. Luyendyk, R. R. Terres, and M. J. Kamerling (1986), Timing and extent of Neogene tectonic rotation in the western Transverse Ranges, California, *Geol. Soc. Am. Bull.*, *97*, 1476–1487.

Huismans, R. S., and C. Beaumont (2003), Symmetric and asymmetric lithospheric extension: Relative effects of frictional-plastic and viscous strain softening, *J. Geophys. Res.*, *108*(B10), 2496, doi:10.1029/2002JB002026.

Hwang, Y. K., J. Ritsema, and S. Goes (2011), Global variation of body-wave attenuation in the upper mantle from teleseismic P wave and S wave spectra, *Geophys. Res. Lett.*, *38*, L08311, doi:10.1029/2011GL046812.

Jennings, C. W., and J. S. George (1994), Fault activity map of California and adjacent areas, with locations and ages of recent volcanic eruptions, scale 1:750 000, Calif. Dep. of Conserv., Div. of Mines and Geol., Sacramento, Calif.

Kennett, B. L. N., E. R. Engdahl, and R. P. Buland (1995), Constraints on seismic velocities in the Earth from travel times, *Geophys. J. Int.*, *122*, 108–124, doi:10.1111/j.1365-246X.1995.tb03540.x.

Langston, C. A., and J. K. Hammer (2001), The vertical component P-wave receiver function, *Bull. Seismol. Soc. Am.*, *91*, 1805–1819, doi:10.1785/0120000225.

LB3D (2013), Long Beach 3D Seismic Array - Teleseismic Data. Caltech. Dataset. doi:10.7909/C3CC0XM7.

Leahy, G., R. Saltzer, and J. Schmedes (2012), Imaging the shallow crust with teleseismic receiver functions, *Geophys. J. Int.*, *191*(2), 627–636.

Legg, M. R. (1991), Developments in understanding the tectonic evolution of the California Continental Border- land, in *From shoreline to abyss; contributions in marine geology in honor of Francis Parker Shepard*, SEPM (Society for Sedimentary Geology) Special Publication, vol. 46, edited by R. H. Osborne, pp. 291–312, SEPM, Tulsa, Okla.

Lekic, V., S. W. French, and K. M. Fischer (2011), Lithospheric thinning beneath rifted regions of southern California, *Science*, *334*(6057), 783–787, doi:10.1126/science.1208898.

Lerner-Lam, A. L., A. F. Sheehan, S. Grand, E. Humphreys, K. Dueker, E. Hessler, H. Guo, D. Lee, and M. Savage (1998), Deep Structure beneath the Southern Rocky Mountains from the Rocky Mountain Front Broadband Seismic Experiement, *Rocky Mt. Geol.*, *33*, 199–216.

Levander, A., E. D. Humphreys, G. Ekstrom, A. S. Meltzer, and P. M. Shearer (1999), Proposed project would give unprecedented look under North America, *Eos Trans. AGU*, *80*(245), 250–251.

Li, X.-Q., and J. L. Nabelek (1999), Deconvolution of teleseismic body waves for enhancing structure beneath a seismic array, *Bull. Seismol. Soc. Am.*, *89*, 190–201.

Lin, F.-C., D. Li, R. W. Clayton, and D. Hollis (2013), High-resolution 3D shallow crustal structure in Long Beach, California: Application of ambient noise tomography on a dense seismic array, *Geophysics*, *78*(4), Q45–Q56, doi:10.1190/geo2012-0453.1.

Luyendyk, B. P. (1991), A model for Neogene crustal rotations, transtension, and transpression in southern California, *Geol. Soc. Am. Bull.*, *103*, 1528–1536.

McNeilan, T. W., T. K. Rockwell, and G. S. Resnick (1996), Style and rate of Holocene slip, Palos Verdes fault, southern California, *J. Geophys. Res.*, *101*(B4), 8317–8334, doi:10.1029/95JB02251.

Meade, B. J., and B. H. Hager (2005), Block models of crustal motion in southern California constrained by GPS measurements, *J. Geophys. Res.*, *110*, B03403, doi:10.1029/2004JB003209.

Mercier, J. P., M. G. Bostock, and A. M. Baig (2006), Improved Green's functions for passive source structural studies, *Geophysics*, *71*(4), SI95–SI102, doi:10.1190/1.2213951.

Miller, K. (2002), Geophysical evidence for Miocene extension and mafic magmatic addition in the California Continental Borderland, *Geol. Soc. Am. Bull.*, *114*(4), 497–512.

Moos, D., and M. D. Zoback (1983), In situ studies of velocity in fractured crystalline rocks, *J. Geophys. Res.*, *88*(B3), 2345–2358, doi:10.1029/JB088iB03p02345.

Mukerji, T., and G. Mavko (1994), Pore fluid effects on seismic velocity in anisotropic rocks, *Geophysics*, *59*(2), 233–244, doi:10.1190/1.1443585.

Nabelek, J. L., X.-Q. Li, S. Azevedo, J. Braunmiller, A. Fabritius, B. Leither, A. Trehu, and G. Zandt (1993), A high resolution image of the Cascadia subduction zone from teleseismic converted phases recorded by a broad-band seismic array, *Trans. Am. Geophys. Union*, *74*, 431.

Nazareth, J. J., and R. W. Clayton (2003), Crustal structure of the Borderland-continent transition zone of southern California adjacent to Los Angeles, *J. Geophys. Res.*, *108*(B8), 2404, doi:10.1029/2001JB000223.

Nicholson, C., C. C. Sorlien, T. Atwater, J. C. Crowell, and B. P. Luyendyk (1994), Microplate capture, rotation of the western Transverse Ranges, and initiation of the San Andreas transform as a low angle fault system, *Geology*, *22*, 491–495, 1994.

Nolet, G., and F. A. Dahlen (2000), Wave front healing and the evolution of seismic delay times, *J. Geophys. Res.*, *105*(B8), 19,043–19,054, doi:10.1029/2000JB900161.

Nowack, R., S. Dasgupta, G. Schuster, and J.-M. Sheng (2006), Correlation migration using Gaussian beams of scattered teleseismic body waves, *Bull. Seismol. Soc. Am.*, *96*, 1–10.

Platt, J. P. (1976), The petrology, structure, and geologic history of the Catalina Schist terrain, southern California, *Univ. Calif. Publ. Geol. Sci.*, *112*, 1–111.

Powell, R. E. (1993), Balanced palinspastic reconstruction of pre-late Cenozoic paleogeology, southern California: Geologic and kinematic constraints on evolution of the San Andreas fault system, *Geol. Soc. Am. Mem.*, *178*, 1–106.

Richards-Dinger, K. B., and P. M. Shearer (1997), Estimating crustal thickness in southern California by stacking Pmp arrivals, *J. Geophys. Res.*, *102*(B7), 15, 211–15, 224.

Roecker, S., B. Baker, and J. McLaughlin (2010), A finite-difference algorithm for full waveform teleseismic tomography, *Geophys. J. Int.*, *181*, 1017–1040.

Ruigrok, E., X. Campman, D. Draganov, and K. Wapenaar (2010), High-resolution lithospheric imaging with seismic interferometry, *Geophys. J. Int.*, *183*, 339–357, doi:10.1111/j.1365-246X.2010.04724.x.

Schmandt, B., and E. Humphreys (2010), Seismic heterogeneity and small-scale convection in the southern California upper mantle, *Geochem. Geophys. Geosyst.*, *11*, Q05004, doi:10.1029/2010GC003042.

Simons, M., et al. (2011), The 2011 magnitude 9.0 Tohoku−Oki Earthquake: Mosaicking the megathrust from seconds to centuries, *Science*, *332*, 1421–1425, doi:10.1126/science.1206731.

Stephenson, W. J., T. K. Rockwell, J. K. Odum, K. M. Shedlock, and D. A. Okaya (1995), Seismic reflection and geomorphic characterization of the onshore Palos Verdes fault zone, Los Angeles, California, *Bull. Seismol. Soc. Am.*, *85*(3), 943–950.

Tape, C., Q. Liu, A. Maggi, and J. Tromp (2009), Adjoint tomography of the southern California crust, *Science*, *325*, 988–992, doi:10.1126/science.1175298.

Tape, C., A. Plesch, J. H. Shaw, and H. Gilbert (2012), Estimating a continuous Moho surface for the California Unified Velocity Model, *Seismol. Res. Lett.*, *83*, 728–735.

ten Brink, U. S., N. Shimizu, and P. C. Molzer (1999), Plate deformation at depth under northern California: slab gap or stretched slab?, *Tectonics*, *18*, 1084–1098.

ten Brink, U. S., J. Zhang, T. M. Brocher, D. A. Okaya, K. D. Klitgord, and G. S. Fuis (2000), Geophysical evidence for the evolution of the California Inner Continental Borderland as a metamorphic core complex, *J. Geophys. Res.*, *105*(B3), 5835–5857.

Thomson, D. J. (1982), Spectrum estimation and harmonic analysis, *Proc. IEEE*, *70*(9), 1055–1096.

Tseng, T.-L., and W.-P. Chen (2006), Probing the Southern Indian Shield with P-wave receiver-function profiles, *Bull. Seismol. Soc. Am.*, *96*(1), 328–333, doi:10.1785/0120050074.

VanDecar, J., and R. Crosson (1990), Determination of teleseismic relative phase arrival times using multi-channel cross-correlation and least squares, *Bull. Seismol. Soc. Am.*, *80*(1), 150–159.

van der Hilst, R. D., B. L. N. Kennett, D. Christie, and J. Grant (1994), SKIPPY: Mobile broadband arrays to study the seismic structure of the lithosphere and mantle beneath Australia, *Eos Trans. AGU*, *75*, 177–181.

Vedder, J. G., D. G. Howell, and J. A. Forman (1979), Miocene strata and their relation to other rocks Santa Catalina Island, California, in *Cenozoic paleogeography of the western United States*, vol. 3, edited by J. M. Armentrout, M. R. Cole, and H. TerBest Jr., pp. 239–256, Society of Economic Paleontologists and Mineralogists, Pacific Coast Paleogeography Symposium, Los Angeles, Calif.

Wald, L. A., L. K. Hutton, and D. D. Given (1995), The southern California network bulletin: 1990-1993 summary, *Seism. Res. Lett.*, *66*, 9–19.

Wang, Z. (2002), Seismic anisotropy in sedimentary rocks, Part 2: Laboratory data, *Geophysics*, *67*, 1423–1440.

Ward, S. N., and G. Valensise (1994), The Palos Verdes terraces, California: Bathtub rings from a buried reverse fault, *J. Geophys. Res.*, *99*(B3), 4485–4494.

Wilson, D. S., P. A. McCrory, and R. G. Stanley (2005), Implications of volcanism in coastal California for the Neogene deformation history of western North America, *Tectonics*, *24*, TC3008, doi:10.1029/2003TC001621.

Wright, T. L. (1991), Structural geology and tectonic evolution of the Los Angeles basin, California, in Active Margin Basins, edited by K. T. Biddle, *Mem. Am. Assoc. Pet. Geol.*, *52*, 35–134.

Yan, Z., and R. W. Clayton (2007a), Regional mapping of the crustal structure in southern California from receiver functions, *J. Geophys. Res.*, *112*, B05311, doi:10.1029/2006JB004622.

Yan, Z., and R. W. Clayton (2007b), A notch structure on the Moho beneath the eastern San Gabriel Mountains, *Earth Planet. Sci. Lett.*, *260*, 570–581.

Yang, Y., and D. W. Forsyth (2006), Rayleigh wave phase velocities, small-scale convection, and azimuthal anisotropy beneath southern California, *J. Geophys. Res.*, *111*, B07306, doi:10.1029/2005JB004180.

Yang, Z., A. F. Sheehan, W. L. Yeck, K. C. Miller, E. A. Erslev, L. L. Worthington, and S. H. Harder (2012), Imaging basin structure with teleseismic virtual source reflection profiles, *Geophys. Res. Lett.*, *39*, L02303, doi:10.1029/2011GL050035.

Yerkes, R. F., T. H. McCullough, J. E. Schoellhamer, and J. G. Vedder (1965), Geology of the Los Angeles Basin, California—An introduction, *U.S. Geol. Surv. Prof. Pap.*, *420–A*, 1–57.

Zhu, L., and H. Kanamori (2000), Moho depth variations in southern California from teleseismic receiver functions, *J. Geophys. Res.*, *105*(B2), 2969–2980.